2010

Development of a three-axis MEMS accelerometer

Jacob Leveto

Development of a Three-Axis MEMS Accelerometer

By

Jacob A Leveto

A Thesis Submitted

in Partial Fulfillment

of the Requirements for the Degree of

Master of Science

in

Microelectronic Engineering

Approved by:

Prof. _____
Dr. Lynn F. Fuller (Thesis Advisor)

Prof. _____
Dr. Robert E Pearson (Thesis Committee Member)
(Microelectronic Engineering MS Program Director)

Prof. _____
Dr. Karl D. Hirschman (Thesis Committee Member)

Prof. _____
Dr. Sohail Dianat (Electrical and Microelectronic Engineering Department Head)

DEPARTMENT OF MICROELECTRONIC ENGINEERING

COLLEGE OF ENGINEERING

ROCHESTER INSTITUTE OF TECHNOLOGY

ROCHESTER, NEW YORK

June, 2010

Development of a Three-Axis MEMS Accelerometer

By

Jacob A Leveto

Signature of Author: _____ Date: _____

ACKNOWLEDGMENTS

I would like to thank my advisor, Dr. Lynn Fuller, for his help and guidance throughout the entire project. Your knowledge of MEMS is unrivaled, and I've learned something new from you almost every day. I would also like to thank my other committee members, Dr. Robert Pearson and Dr. Karl Hirschman, for their support throughout my graduate studies. Both my class and co-op schedule over the past five years have be anything but typical, however with their guidance I was able to finish both my undergraduate and graduate degree in a short period of time. Special thanks to Ivan Puchades, whose MEMS processing knowledge, design experience, and willingness to help have saved me from several critical mistakes.

This project wouldn't have been possible without the help of the Semiconductor and Microsystems Fabrication Laboratory staff. I would like to give specific thanks to Sean O'Brien, David Yackoff, Rich Battaglia, John Nash, and Bruce Tolleson. These men always kept the tools running and helped me on several occasions when the tools failed to cooperate. Thanks to Tom Grimsley for processing my mask set while simultaneously processing all of the other senior design mask sets.

Finally I would like to thank all of the microelectronic engineering faculty members who have made this journey before, and the students who are making it with me now. Engineering requires building upon previous knowledge as well as collaboration with other engineers. I couldn't have made it alone, thanks for your support.

ABSTRACT

While originally developed to deploy air bags for the automotive industry, Microelectromechanical Systems (MEMS) based accelerometers have found their way into everything from video game controllers to cells phones. As prices drop and capabilities improve, it is expected that the use of accelerometers will further expand in the coming years. Accelerometers currently have the second highest MEMS sales volume, trailing only pressure sensors [1]. In this work several single and three-axis accelerometers are designed, fabricated, and tested under a variety of conditions.

The designed accelerometers are all based off of the piezoresistive effect, where the value of a resistor changes with applied mechanical stress [2]. When accelerated, the inertia of a suspended proof mass causes stress on piezoresistors placed on support arms. The corresponding changes in these resistor values are then converted to an output voltage using a Wheatstone bridge. To sense acceleration independently in all three axes, structures with three distinct modes of vibration and three sets of Wheatstone bridges are used.

Devices were fabricated at the Semiconductor and Microsystems Fabrication Laboratory (SMFL), located at RIT. A modified version of the RIT bulk MEMS process was used, consisting of 65 steps, 7 photolithography masks, bulk silicon diaphragm etch, and top hole release etch [3].

Unfortunately the finished chips show poor aluminum step coverage into contact vias and over polysilicon lines. This results in open circuits throughout the chip, prohibiting proper operation. Process corrections have been identified, and with proper fabrication the designs are still expected to yield working devices. Since the finished

accelerometers were not functional, several commercial accelerometers have been tested to characterize sensitivity, linearity, cross-axis sensitivity, frequency response, and device lifetime.

TABLE OF CONTENTS

Title Page..... i
Library Release Page..... ii
Acknowledgement..... iii
Abstract..... iv
Table of Contents..... v
List of Tables..... viii
List of Figures..... ix
List of Acronyms..... xii
Chapter 1 Introduction..... 1
1.1 Motivation..... 1
1.2 Partnership with Impact..... 2
Chapter 2 Current Technology and Research..... 3
2.1 Piezoresistive Technology..... 3
2.1.1 Strain Fundamentals..... 6
2.2 Capacitive Technology..... 10
2.3 General Accelerometer Considerations..... 12
Chapter 3 Simulation..... 15
3.1 Finite Element Analysis..... 15
3.2 Process Simulation..... 18
Chapter 4 Design..... 20
4.1 Device Designs..... 20
4.1.1 Dual Rectangular Structure..... 22
4.1.2 Monolithic Structure #1..... 24
4.1.3 Monolithic Structure #2..... 26
4.2 Piezoresistor Bridge Configuration..... 27
4.3 Physical Dimensions, Materials, and Sensitivities..... 28
4.4 Process Constraints..... 29
Chapter 5 Fabrication..... 31
5.1 Bulk MEMS Process Flow..... 31
5.2 Processing Issues..... 38
5.3 Finished Devices..... 44
Chapter 6 Testing..... 46
6.1 Introduction..... 46
6.2 Methods..... 47
6.3 Amplification..... 53
6.4 Sensitivity..... 55
6.5 Linearity..... 60
6.6 Cross-Axis Sensitivity..... 61
6.7 Frequency Response..... 64
6.8 Mechanical Stability..... 67
Chapter 7 Conclusion..... 68
7.1 Introduction..... 68
7.2 Future Work..... 68

Appendices..... 70
Appendix 1 - RIT Bulk MEMS Process Flow 70
Appendix 2 – Full bridge behavior under all acceleration conditions..... 71
Appendix 3 – Silvaco Athena Simulations..... 72
Appendix 4 – Micrograph of the three-axis accelerometer..... 73
References..... 74

LIST OF TABLES

Table 1– Sample of current academic piezoresistive accelerometer research 5
Table 2 - Piezoresistance coefficients for the <110> direction, units of 10^{-11} Pa^{-1} [17] 7
Table 3 – Schematic layers and colors 21
Table 4 – Dual rectangular bridge resistor changes under X, Y, and Z acceleration. 28
Table 5 – Monolithic structure #1-2 bridge resistor changes under X, Y, and Z acceleration. Differences from Table 4 in Z bridge under X acceleration 28
Table 6 – Theoretical piezoresistive coefficients and sensitivities for the fabricated accelerometers. Unlisted sensitivities were not simulated and should be lower than the less aggressive versions. 29
Table 7 – Device dimensions along with simulated resonant frequencies. Unlisted frequencies were not simulated but should be higher than the less aggressive versions. 29
Table 8 – Tested accelerometers 46

LIST OF FIGURES

Figure 1 – Basic cantilever model for 1-axis detection [6] 4
Figure 2 - Monolithic three-axis accelerometer from Takao *et al.* [7] 4
Figure 3 - First commercialized MEMS accelerometer from Roylance *et al.* [9] 5
Figure 4 – RIT Fabricated accelerometer and results [16] 6
Figure 5– Piezoresistance factor $P(N,T)$ for p-Si as a function of doping and temperature [19]. 8
8
Figure 6 – Piezoresistance coefficients at room temperature for the (001) plane of p-Si [19].
Figure 7 - Valance band warping and splitting under strain [17]. 9
Figure 8 – Three-axis capacitive accelerometer from Eklund *et al.* [23] 11
Figure 9 – Simulated Coefficient of Sensitivity (TCS) results, sensitivity decreases as temperature increases [29] 13
Figure 10 – Examples of optical and tunneling accelerometers [5] 14
Figure 11 – Dual rectangular design 16
Figure 12 – Simulations of the dual rectangular structure at 1 g of acceleration in the Z (left) and X/Y (right) directions. 16
Figure 13 - Simulations of the monolithic structure #1 at one g of acceleration in each direction. 17
Figure 14 – Simulations of the monolithic structure #2 at one g of acceleration in each direction. 17
Figure 15 – Silvaco Athena simulations of a 10 μm wide p+ diffused resistor. 2D profile (left) and vertical cutline (right). Simulations predict a sheet resistance of 523 Ω/□ 18
Figure 16 - Silvaco Athena simulations of a 640 μm wide p+ diffused resistor. Simulations predict a sheet resistance of 538 Ω/□ 19
Figure 17 – 4" Contact alignment mask layout with all device designs and alignment marks. 21
22
Figure 18 – 4x4 mm test structure. Includes connections over the n- substrate, p+ implant (narrow and wide), n+ polysilicon, and aluminum layers.
23
Figure 19 – Mask layout of the original dual rectangular structure, designed in the winter 2009-2010 quarter.
Figure 20 – Dual rectangular design with Wheatstone bridge resistor overlays 23
Figure 21 - Mask layout of the improved dual rectangular structure, designed in spring 2010. 24
Figure 22 – Mask layout of the high sensitivity monolithic structure #1. A lower sensitivity version with wider support arms and polysilicon piezoresistors is also fabricated. 25
Figure 23 - Monolithic structure #1 with three Wheatstone bridges overlaid 25
Figure 24 - Mask layout of the low sensitivity monolithic structure #2. A higher sensitivity version with more narrow support arms and p+ diffused piezoresistors is also fabricated. 26

Figure 25 – Monolithic structure #2 with three Wheatstone bridges overlaid 27
Figure 26 – Bridge configuration for all three axes. See Appendix 2 for 28
Figure 27 – Cross-section after RIT bulk MEMS processing [2] 30
Figure 28 – RIT Bulk MEMS Process – Ready for p+ diffusion 32
Figure 29 – RIT Bulk MEMS Process – After n+ diffusion 32
Figure 30 – RIT Bulk MEMS Process – Backside nitride deposited 33
Figure 31 – RIT Bulk MEMS Process – Backside alignment 33
Figure 32 – RIT Bulk MEMS Process – Diaphragm hard mask etched 34
Figure 33 – RIT Bulk MEMS Process – Doped polysilicon deposited 34
Figure 35 – RIT Bulk MEMS Process – Metal1 35
Figure 34 – RIT Bulk MEMS Process – ILD2 deposited 35
Figure 36 – RIT Bulk MEMS Process – Metal 2 deposited 36
Figure 37 – Lateral KOH etch (bottom) and Reactive Ion Etch (RIE) (top). 37
λ = 10 μm, diaphragm thickness = 30 μm.
Figure 38 – RIT Bulk MEMS Process – Diaphragm etched 37
Figure 39 – RIT Bulk MEMS Process – Finished devices 38
Figure 40 – Secondary Electron Micrograph (SEM) of poor aluminum step 40
coverage over polysilicon lines (left) and into a contact via (right).
Figure 41 – Aluminum step coverage without (left) and with (right) a heated 41
substrate [31]
Figure 42 – Aluminum step coverage without (left) and with (right) a 75V RF 41
bias sputter [31]
Figure 43 – Finished three-axis accelerometers. Monolithic structure #2 (left) 44
and dual rectangular structure (right). The black area represents the top hole
release etch.
Figure 44 – One-axis accelerometers also fabricated on the same wafers. 45
Figure 45 - Tested Accelerometer, listed from left to right, ADXL30 in the 46
iPhone, LIS331DL in the Wiimote, ADXL278, Minisense 100, ADXL330, and
BMA 140.
Figure 46 – Low g accelerometer testing units [6]. 48
Figure 47 – Speaker accelerometer testing unit 49
Figure 48 – Measuring maximum displacement of the speaker to calculate 49
theoretical acceleration
Figure 49 – Permanent Magnet Shaker 50
Figure 50 – Rotation test around the x-axis and sample results. The two sine 51
waves show Y and Z acceleration while noise shows possible X acceleration due
to axis cross talk
Figure 51 – Two orthogonal PM-Shakers for cross-axis sensitivity measurement 51
[36]
Figure 52 – Possible examples of non-linearity using the testing methods above 52
Figure 53 – Custom built three-channel instrumentation amplifier PCB (left) 54
along with one of several carrier boards (right). Each channel has variable gain
and contains the INA101 high precision instrumentation amplifier chip [38].
Figure 54 – Gain as a function of reference resistor value for each channel. 54
Follows Equation 15
Figure 55 – Frequency response of the amplifier set to 1000X gain. 20dB/decade 55

roll off starts at 2 kHz
Figure 56 – Wiimote accelerometer measured with reference to the iPhone accelerometer. Measured at 8 Hz on the speaker setup 56
Figure 57 – Impulse event of a half sine wave at 1000 Hz on the iPhone (left) and Wiimote (right). 57
Figure 58 – AC Power noise while measuring the idle Minisense 100. 57
Figure 59 – Output voltages of the Analog Devices ADXL278 and Minisense 100 accelerometers while driven at 40 Hz. 58
Figure 60 – Minisense 100 sensitivity at 40 Hz 59
Figure 61 – iPhone under acceleration from the cantilever setup. A truly sinusoidal response is measured. Shown again with a closer view in Figure 62 59
Figure 62 – Acceleration and vertical velocity of the iPhone when tested on the cantilever. 60
Figure 63 – Acceleration measurements of the iPhone sitting flat on a level table 61
Figure 64 – Acceleration measurements (left) and cross-axis sensitivity levels (right) of the iPhone being rotated around the y-axis (top) and x-axis (bottom) 62
Figure 65 – Speaker with attached Nintendo Wiimote and Apple iPhone 63
Figure 66 – Cantilever introducing axis cross talk at high amplitude 64
Figure 67 – Frequency response of the Minisense accelerometer as shown by the manufacturer [39] 64
Figure 68 – Measured frequency response of the Minisense accelerometer. Resonance occurs at 61 Hz. Tested on the speaker setup with 100 mV of sinusoidal input 65
Figure 69 – Impulse on the Minisense reveals a resonant frequency of 63 Hz 66
Figure 70 – Frequency response of the speaker-accelerometer system. iPhone shows distinct beats near the half and full sampling frequency, as shown in Figure 71. 67
Figure 71 – Beats near the sampling frequency (100 Hz), distorting the frequency response results. 67
Figure 72 – Output voltage of the Minisense accelerometer while excited at ±23.6 g for 24 hours. No difference measured 69
Figure 73 – PCB Schematic to test the Analog Devices ADXL330 and Bosch BMA140 accelerometers 69

LIST OF ACRONYMS

ALD	Atomic Layer Deposition
BOE	Buffered Oxide Etch
CKEM	Compact Kinetic Energy Missile
CMP	Chemical Mechanical Planarization
FEA	Finite Element Analysis
FEM	Finite Element Method
GF	Gauge Factor
HF	Hydrofluoric Acid
ILD	Inter Level Dielectric
LC	Inductive-Capacitive
LPCVD	Low Pressure Chemical Vapor Deposition
LTO	Low Temperature Oxide
KOH	Potassium Hydroxide
MEMS	Microelectromechanical System
MGSL	Maximum G Sensing Level
MOCVD	Metal Organic Chemical Vapor Deposition
MOSFET	Metal Oxide Semiconductor Field Effect Transitor
PCB	Printed Circuit Board
PECVD	Plasma Enhanced Chemical Vapor Deposition
PM-Shaker	Permanent Magnet Shaker
PVD	Physical Vapor Deposition
RCA	Radio Corporation of America (RCA-Clean)
RIE	Reactive Ion Etch
RIT	Rochester Institute of Technology
RF	Radio Frequency
SEM	Scanning Electron Microscope, Scanning Electron Micrograph
SMD	Surface Mounted Device
SOI	Silicon On Insulator
SMFL	Semiconductor Manufacturing and Fabrication Laboratory
TCO	Temperature Coefficient of Offset
TCS	Temperature Coefficient of Sensitivity
TEOS	Tetraethyl Orthosilicate

Chapter 1

Introduction

1.1 Motivation

Microelectromechanical Systems (MEMS) is currently one of the fastest growing fields in the microelectronics industry. Accelerometers in specific have the second highest sales volume after pressure sensors [1], and sales continue to increase as more applications emerge. One of the original driving forces of MEMS based accelerometers has been the automotive industry, which uses accelerometers for stabilization, suspensions, and most importantly their air bag deploying systems. In addition to automotive applications, accelerometers are now being used in consumer electronics, including but not limited to game controllers, laptops, and cell phones. Accelerometers are widely used in machine health monitoring, where early vibration detection can signal a faulty part before catastrophic breakdown. Highly sensitive accelerometers can be used to measure extremely precise quantities such as gravitational field strength and small earthquakes. Many of these applications are not possible with conventional non-MEMS based accelerometers due to size and cost, as it would not be practical to put a conventional accelerometer in a cell phone.

One useful MEMS device that could be fabricated is a multi-sensor chip that contains several sensors on the same die, including temperature, humidity, acceleration, stress, and pH. The current RIT bulk MEMS process is capable of making all of these devices on the same chip [2]. Combining these sensors along with the required electronics onto a single die will save money, add functionality, and reduce the overall footprint of the device.

While this project is primarily based upon microelectronic engineering principles that are used to fabricate the device, it also requires several other disciplines. Mechanical engineering is required to describe the motion and forces within the system. Electrical engineering is needed to condition, amplify, and output a readable signal. Finally, good communications skills are needed to share results with other engineers.

1.2 Partnership with Impact

Several military agencies have recently shown an increased interest in MEMS sensors [3]. Predictions of the remaining life of a system can be greatly aided with historical temperature, humidity, vibration, and stress data. RIT has partnered with Impact Technologies on several prognostic sensors, most of which would benefit from a three-axis accelerometer. It is possible that future projects at both RIT and Impact could benefit from this work. Other military projects, such as the Compact Kinetic Energy Missile (CKEM), require high performance accelerometers capable of operating through launch accelerations as high as 1000 gs [4]. Proprietary and non-public information on these projects will not be discussed in this document.

Chapter 2

Current Technology and Research

2.1 Piezoresistive Technology

Most piezoresistive designs consist of a proof mass (*m*), elastic spring (*k*) with an attached resistor, and damping medium (*b*), usually air [1], [5]. These forces can be modeled as an under-damped simple harmonic oscillator, with the force balance given by Equation 1, where *a* is acceleration and *x* is displacement. When acceleration is applied to the sensor, the inertia of the proof mass applies force to the spring. The spring then deforms, exerting stress on an attached resistor. The resistor changes resistance due to the applied stress, which can be converted to a readable voltage using a Wheatstone bridge. The system then oscillates in a sinusoidal manner until damping returns it to equilibrium. Figure 1 shows an example of a basic cantilever approach, capable of detecting acceleration in one direction, while Figure 2 shows a design capable of independently detecting all three axes of acceleration. The three-axis accelerometer is able to independently oscillate up and down to sense z-acceleration, rotate left and right to detect x-acceleration, and rotate forward and backwards to detect y-acceleration.

$$m\frac{d^2x}{dt^2} + b\frac{dx}{dt} + kx = ma \qquad 1$$

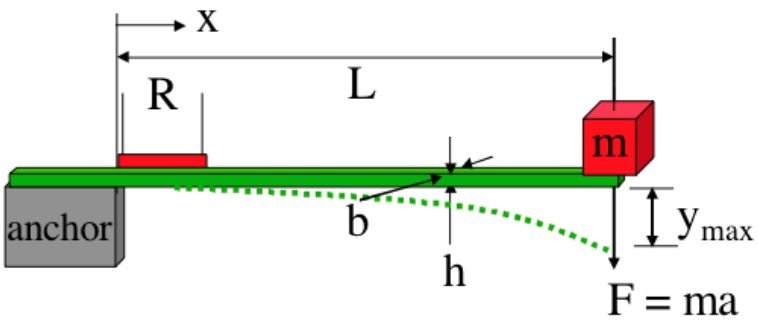

Figure 1 – Basic cantilever model for 1-axis detection [6]

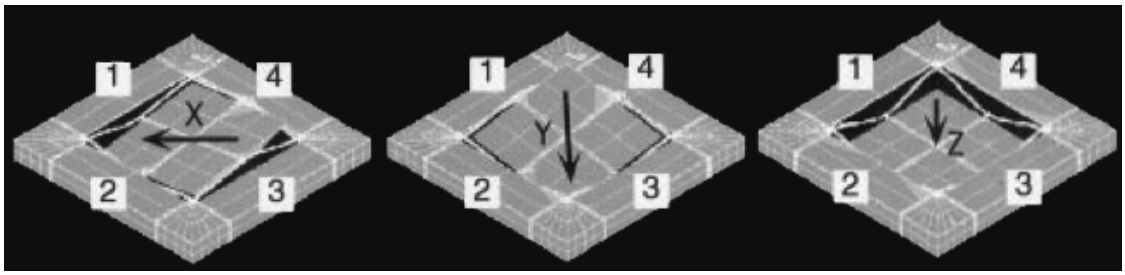

Figure 2 - Monolithic three-axis accelerometer from Takao *et al.* [7]

The main attraction of piezoresistive sensors is the simplicity of their design and fabrication, with one specific process using only a single mask [8]. Readout circuitry is often much simpler and based off of a resistive bridge and amplifier. Piezoresistive accelerometers suffer from larger temperature variation and lower sensitivity compared to capacitive based designs. This suits piezoresistive sensors to high-g and low-sensitivity applications. For example, piezoresistive sensors may be better suited for an airbag deploying system, while capacitive sensors may work better for motion controlled input devices.

The first commercial MEMS accelerometer was piezoresistive based and used a bulk micromachining process. The structure, shown in Figure 3, was developed in 1979 by Roylance *et al.* [9]. It is capable of sensing one-axis of acceleration from 0.001 to 50 g, with a 100 Hz bandwidth.

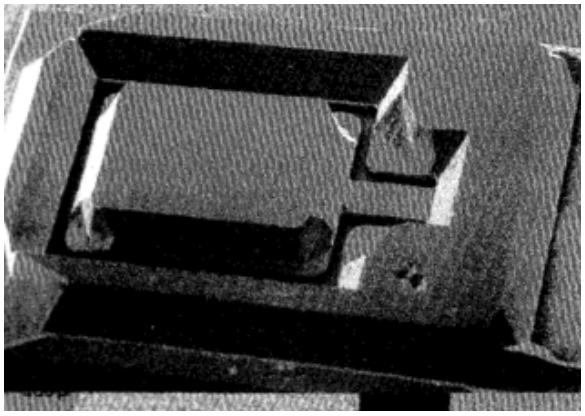

Figure 3 - First commercialized MEMS accelerometer from Roylance *et al.* [9]

Table 1 gives a summary of recent academic papers published on multi-axis piezoresistive accelerometers. Sensitivities in the μV/gV range indicate that amplification is needed to accurately read the output signals. The linearity, cross-axis sensitivity, and bandwidth values give a good indication of the possible uses of these devices. All of the accelerometers are capable of simple applications such as deploying an airbag, but would be unsuited for high precision applications such as a motion activated video game controller.

Group	Axes	Range [±g]	Sensitivity XY, Z [mV/gV]	Linearity [%]	Cross-Axis Sens. [%]	Bandwidth [kHz]
Kwon, 1998 [10]	2	?	0.23 , 0.79	?	4	6.56
Kal, 1995 [11]	2	13	0.004, 0.11	0.25	?	1.65
Takao, 2001 [7]	3	?	31, 168*	< 1.0	2 to 7	?
Doa, 2004 [12]	3	?	0.09, 0.11	1.0	5.5	4.3
Amarasinghe, 2005 [13]	3	10	0.10, 1.78	1.3	4	2.1
Plaza, 2001 [14]	3	?	0.09, 0.02	0.59	8.8	0.72
Chen, 2008 [15]	2	?	0.90*	0.05	?	0.67

* Supply voltage not given, units of [mV/g]

Table 1– Sample of current academic piezoresistive accelerometer research

Lynn Fuller, Burak Baylav, and Ivan Puchades have previously fabricated several piezoresistive accelerometers at RIT [16]. The device and results, shown in Figure 4, have been demonstrated to work. The signal to noise ratio looks low, partially due to low amplification applied after the signal has traveled through several feet of wiring, along with it's high-g design. It is the goal of this project to improve upon RIT's accelerometers and generate a clean signal under both low and high accelerations.

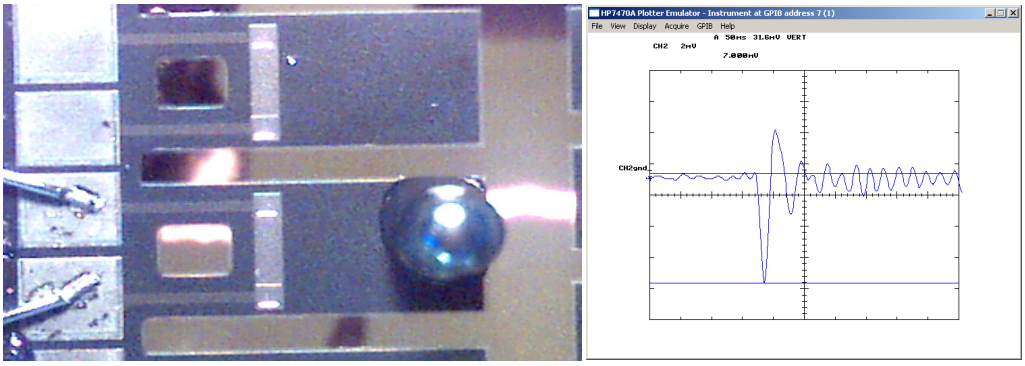

Figure 4 – RIT Fabricated accelerometer and results [16]

2.1.1 Strain Fundamentals

Mechanical stress can be described as the average amount of force exerted per area within a deformable body in which internal forces act. The SI unit for stress is the pascal, where 1 Pa = 1 N/m^2. When stress causes an expanding force on an object it is said to be under tensile strain, when the stress causes a shrinking force it is said to be under compressive strain. Young's Modulus is the ratio of stress to strain, and is given by Equation 2 where σ is stress, ε is strain, and E is the Young's Modulus. Equation 3 shows the elastic deformation of an object related to strain. The Young's Moduli for silicon and germanium are 185 GPa and 103 GPa, respectively.

$$E = \frac{\sigma}{\varepsilon} \quad (2)$$

$$X_{final} = X_{initial}\varepsilon \quad (3)$$

Piezoresistance coefficients are a way to quantify the change in resistivity as a function of strain. This is shown in Equation 4, where ρ is resistance and π is the piezoresistive coefficient. When dealing with strain in crystals, carrier mobility can no longer be considered constant for bulk material. Each conduction direction has it's own set of effective masses and scattering properties, so both parallel ($\pi_{||}$) and perpendicular ($\pi_{\perp}$) piezoresistance coefficients are needed.

$$\Delta\rho = \varepsilon\pi\rho \quad (4)$$

Table 2 shows both the $\pi_{||}$ and $\pi_{\perp}$ coefficients for bulk silicon in the <110> direction, first reported by Smith *et al.* in 1954. From this table it can be shown that hole mobility is increased with uniaxial compressive strain and decreased by uniaxial tensile strain, while electron mobility is decreased by uniaxial compressive strain and increased by uniaxial tensile strain [17], [18].

Polarity	$\pi_{//}$	$\pi_{\perp}$
N	-31.6	-17.6
P	71.8	-66.3

Table 2 - Piezoresistance coefficients for the <110> direction, units of 10^{-11} Pa^{-1} [17]

The values given in Table 2 do not take two-dimensional transport behavior, temperature, doping, or electric field into account. The true piezoresistance coefficient is given by Equation 5, where $P(N,T)$ is the piezoresistance factor, N is doping concentration, and T is temperature [19]. Multiplying the piezoresistance factor N, shown in Figure 5 for p type silicon, and the room temperature piezoresistance coefficient shown in Figure 6, gives the final piezoresistance coefficient as a function of temperature and doping.

$$\Pi(N,T) = P(N,T)\Pi(300\text{K}) \qquad 5$$

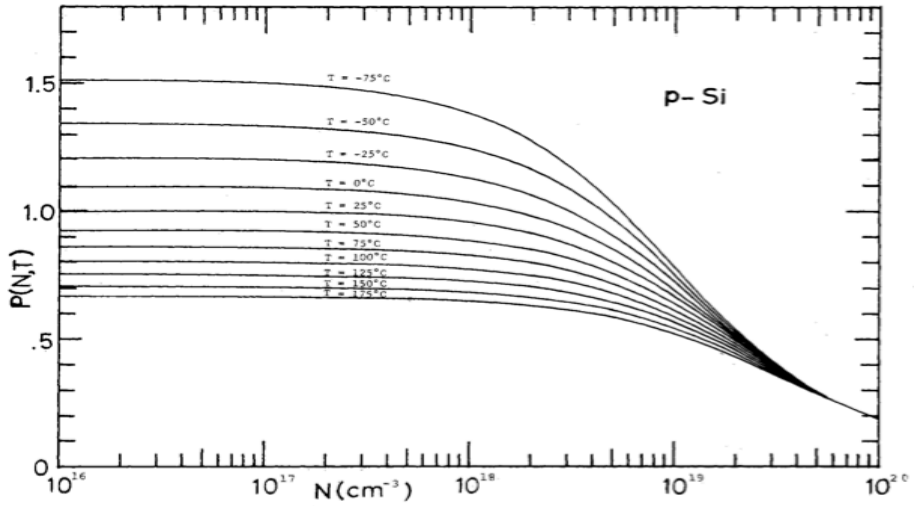

Figure 5– Piezoresistance factor $P(N,T)$ for p-Si as a function of doping and temperature [19].

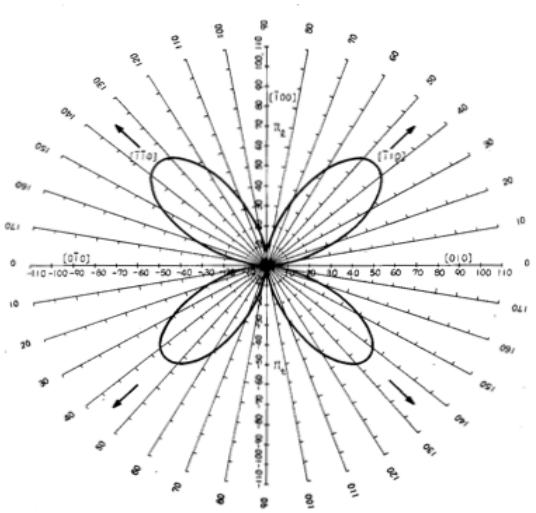

Figure 6 – Piezoresistance coefficients at room temperature for the (001) plane of p-Si [19].

The effects of strain on electron mobility are more widely known due to the conduction band structure being less complicated than that of the valance band. Both uniaxial and biaxial tensile strain in silicon induces splitting of the six-fold conduction band degeneracy between the in-plane and perpendicular valleys. This results in the reduction of intervalley electron scattering along with a decrease in the electron effective mass, both of which increase mobility. For holes, uniaxial compressive strain induces band warpage and the splitting of the light and heavy hole bands, both increasing mobility [20]. Figure 7a shows the three valance bands in unstrained silicon, containing heavy holes, light holes, and split-off holes. Under biaxial strain, Figure 7b shows all three bands rising in energy. It also shows that the light hole band narrows and raises to have the highest energy. Figure 7c shows that when uniaxial strain is applied all bands increase different amounts of energy, but there is no band narrowing like that seen with biaxial strain.

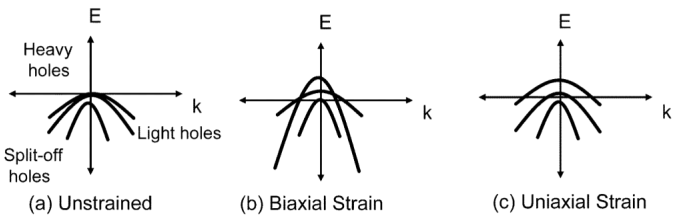

Figure 7 - Valance band warping and splitting under strain [17].

In addition to resistance change based on mobility, physical deformation also changes the overall resistance. A common metric used is the gauge factor (*GF*), given by Equation 6, where ε is strain. Equation 7 gives the change in resistance, where v is the Poisson's ratio of the material and ρ is resistivity [5], [21].

$$GF = \frac{\Delta R}{R}\frac{1}{\varepsilon} \tag{6}$$

$$\frac{\Delta R}{R} = (1 + 2\upsilon)\varepsilon + \frac{\Delta \rho}{\rho} \tag{7}$$

Gauge factors in metals are typically around 2, while lightly doped semiconductors can have factors on the order of 100 [5]. Heavily doped polysilicon typically has lower gauge factors than single crystal silicon due to the low gauge factor of grain boundaries dominating the high gauge factors of the actual grains themselves. Heavily doped polysilicon with large grains can have gauge factors as high as 30 [22].

2.2 Capacitive Technology

Capacitive accelerometers operate with the same mass, spring, and damper model that piezoelectric accelerometers use, but instead of measuring the change in resistance they measure the change in capacitance between parallel plate capacitors. Equation 8 gives the capacitance between two parallel plates, where A is the area, ϵ is the permittivity between the plates, and t is distance between plates. Figure 8 shows a capacitive three-axis accelerometer. Acceleration in the X and Y direction is detected by the variation in t, while Z acceleration is detected by the variation in A.

$$C = \frac{A\varepsilon}{t} \tag{8}$$

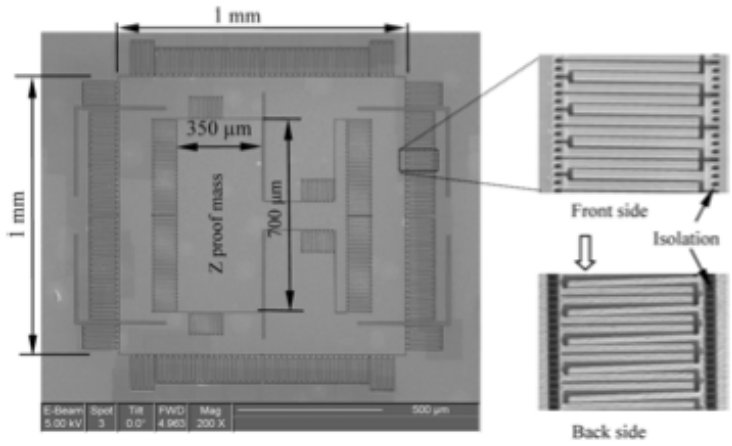

Figure 8 – Three-axis capacitive accelerometer from Eklund *et al.* [23]

Capacitive devices have several advantages over piezoresistive technology. They usually have high precision, low noise, low drift, low temperature sensitivity, and low power consumption. They are however, susceptible to electromagnetic interference, must have more complicated capacitance reading circuitry on chip, and require a more complicated and precise surface micromachining manufacturing process [24].

While piezoresistive sensors typically output a voltage, capacitive sensors have the option of outputting a variable frequency. An inductive-capacitive (LC) oscillator can be created using the variable capacitor to vary frequency, shown in Equation 9, where L is inductance and C is capacitance [25].

$$F = \sqrt{\frac{1}{LC}} \qquad 9$$

Capacitive accelerometers are among the most widely implemented sensors for consumer electronics. Companies such as Analog Devices offer three-axis low-g accelerometers at prices of $2.38 in quantities of 1000 or more [26]. The devices have a wide variety of ranges, varying from ±2 to ±16 g depending on the model. A small form factor of 4x4 mm and wide operating temperature range of -40 to 85°C make these

sensors attractive for cell phones and game controllers. Higher g models are also available, sensing up to ±70 g in one or two axes [27]. Analog Devices is not the only company to produce accelerometers, devices are also available from Silicon Designs, Endevco, Bosch, Freescale, and more. Beliveau *et al.* shows that these capacitive devices usually have very high mechanical stability [28]. The Silicon Designs Inc 1220 accelerometer has a maximum g-sensing level (MGSL) of 3,600 to 5,400 g, while independent tests show first signs of failure past 70,000 g.

2.3 General Accelerometer Considerations

The resonant frequency is an important factor to consider when choosing an accelerometer. MEMS accelerometers are designed to operate below their resonant frequency, where they provide consistent output independent of frequency. As the device approaches resonance even small vibrations will cause the amplitude of the proof mass oscillation to grow considerably, making any output response meaningless.

Variations in temperature can have a large effect on piezoresistive sensors. The Temperature Coefficient of Offset (TCO) is an offset voltage caused by the change in resistance of resistors due to temperature. As long as the Wheatstone bridge is symmetrical, changes cancel and TCO does not pose a problem. The Temperature Coefficient of Sensitivity (TCS) has a much greater influence on performance, and is a result of piezoresistive coefficients being dependent on temperature. Figure 9 shows simulated outputs at varying temperatures. As temperature goes up, sensitivity goes down [29]. This effect must be compensated for, either by analog or digital correction. If the accelerometer is part of a multi-sensor chip, the easiest way is to digitally correct the measured acceleration voltages using data from the temperature sensor.

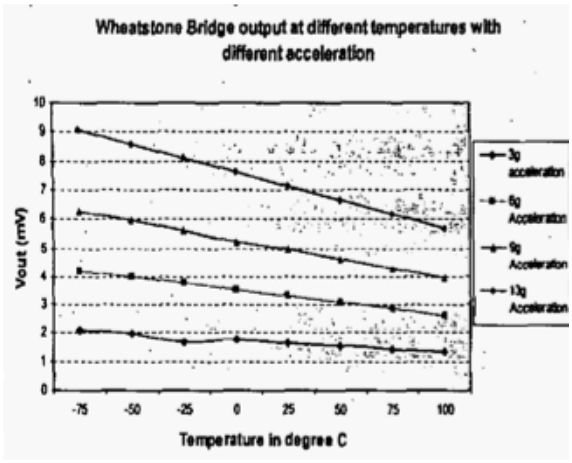

Figure 9 – Simulated Coefficient of Sensitivity (TCS) results, sensitivity decreases as temperature increases [29].

The Finite Element Method (FEM), also referred to as Finite Element Analysis (FEA), is a powerful tool that can be used to simulate accelerometers. After a mesh of the device is constructed and boundary conditions are set, computer simulations solve a set of simultaneous partial differential equations to an acceptable degree of error. From these simulations strain, stress, displacement, and other physical parameters can be modeled over the entire mesh. Similar methods are used to simulate process design and electrical simulations using software such as Silvaco's Athena and Atlas packages.

In addition to piezoresistive and capacitive sensors, several other types exist. Piezoelectric accelerometers are similar in structures to piezoresistive ones, but a special piezoelectric material in place of the piezoresistor generates its own voltage when strained. These devices suffer in that they cannot read steady sources of acceleration, such as earth's gravitational field. Resonant devices actuate at their resonance frequency, stress changes this natural frequency, which is then measured. Optical accelerometers use mechanical movement of a proof mass to modulate light. Light intensity can be measured

and converted to acceleration. Tunneling devices use a feedback loop to maintain a constant current between a tunneling tip and proof mass. Figure 10 shows examples of an optical and tunneling accelerometer.

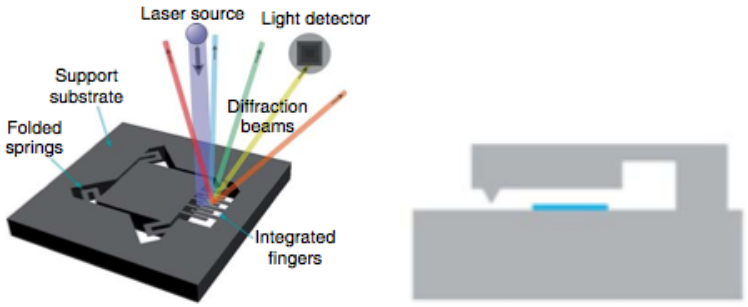

Figure 10 – Examples of optical and tunneling accelerometers [5].

Chapter 3

Simulation

3.1 Finite Element Analysis

Several commercial software packages are capable of simulating MEMS devices, such as ANSYS, COMSOL Multiphysics, and Solidworks to name a few. COMSOL Multiphysics has been chosen due to its capabilities, simplicity, and built in MEMS module designed specifically for simulating MEMS devices. All models have been simulated with 1 g of acceleration in all three directions, as well as analyzed for the first several modes of vibration.

Three different device are designed are investigated, including the dual rectangular structure, monolithic structure #1, and monolithic structure #2. The dual rectangular structure has been through two design-fabrication iterations, while the monolithic structures have only been through one.

Figure 11 shows the designed three-axis accelerometer half structures for the dual rectangular structure. Each of the six support beams is fixed to the bulk of the surrounding chip. Two of these structures, placed perpendicular to one and other, are required to sense acceleration in all three axes. Figure 12 shows the stress distribution of the first two modes of vibration when the model is deformed under 1 g of acceleration in both the Z and Y directions. Maximum stress, strain, and sensitivity values from these simulations are summarized in the next chapter.

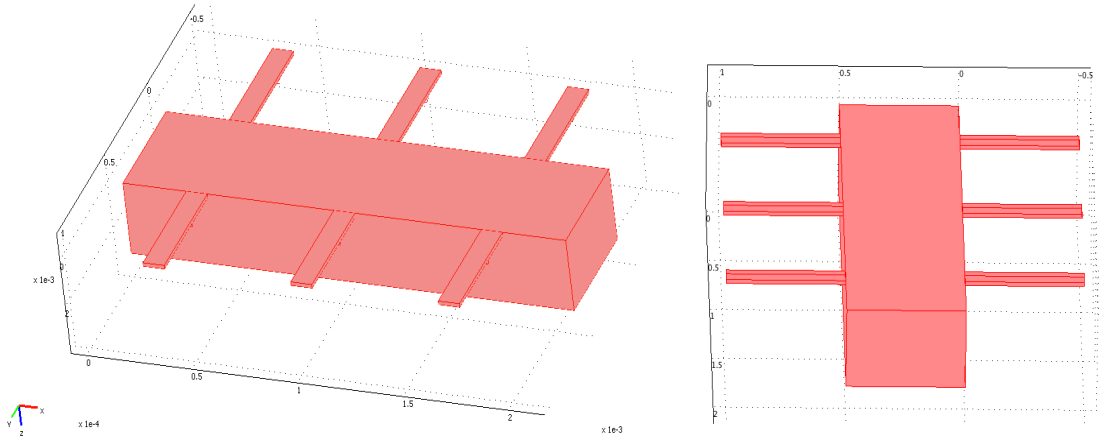

Figure 11 – Dual rectangular design

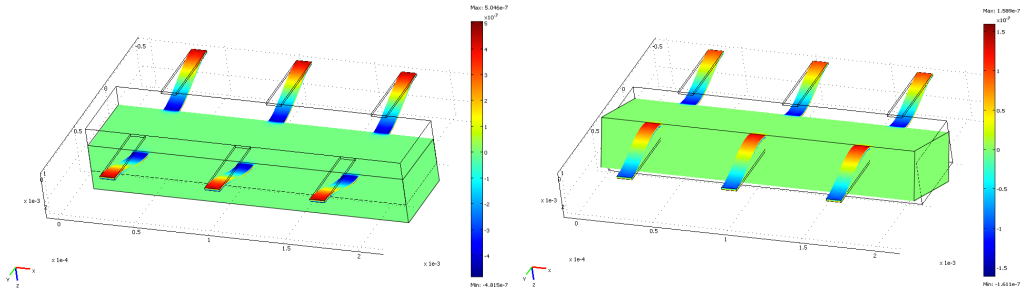

Figure 12 – Simulations of the dual rectangular structure at 1 g of acceleration in the Z (left) and X/Y (right) directions.

Figure 13 and Figure 14 show the monolithic accelerometer structures under their first three modes of acceleration. The first mode has the lowest frequency and corresponds to acceleration in the Z direction. The second and third mode, both of same frequency, corresponds to acceleration in the X and Y directions. The second and third modes of vibration have slightly higher frequencies than the first mode.

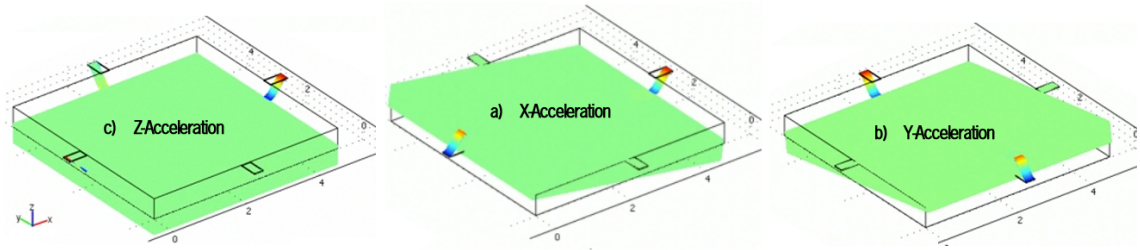

Figure 13 - Simulations of the monolithic structure #1 at one g of acceleration in each direction.

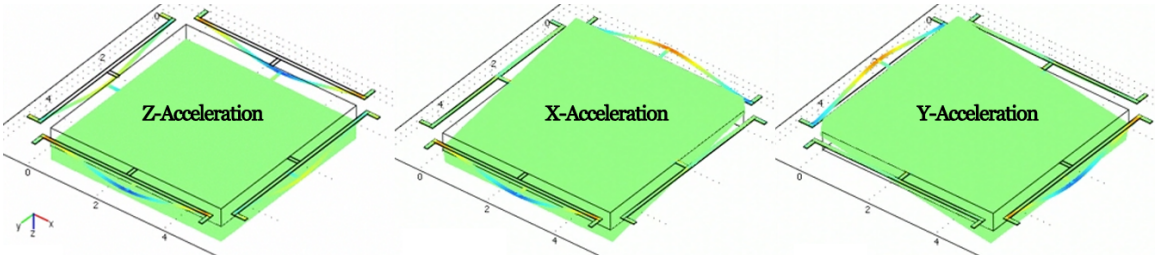

Figure 14 – Simulations of the monolithic structure #2 at one g of acceleration in each direction.

To measure the acceleration using these structures, three Wheatstone bridges are formed on top of the areas of highest strain. The bridges are setup so that each bridge only outputs a voltage when acceleration in the correct direction is applied, and output no voltage when acceleration in the other two directions are applied. For example, the Y-bridge will output a voltage when the device is accelerated in the Y direction, but will outputs no voltage when accelerated in the X and Z direction. This is achieved through a combination of design symmetry, proper piezoresistor placement, and correct configuration of all Wheatstone bridges. All bridge and acceleration combinations are explained in the next chapter and also shown in Appendix 2.

Linearity is a required characteristic of any accelerometer, so output voltage should be directly proportional to acceleration. This is achieved by operating in the

elastic deformation zone of the silicon springs, where stress on the piezoresistors is directly proportional to force applied.

3.2 Process Simulation

To achieve the highest sensitivity levels, the piezoresistive coefficient must be maximized. Maintaining a reasonable doping level around or below 10^{18} cm^{-3} ensures that ionic scattering does not significantly degrade the piezoresistive coefficient. Silvaco's Athena software package is used to model all process steps that effect the final dopant distribution. Both narrow (10 µm) and wide (640 µm) p+ diffused resisters are simulated, with dopant profiles shown in Figure 15 and Figure 16, respectively. These profiles are from the Athena deck shown in Appendix 3. Both simulations result in piezoresistor sheet resistances of around 525 Ω/□, with peak boron concentrations around $3x10^{18}$ cm^{-1}.

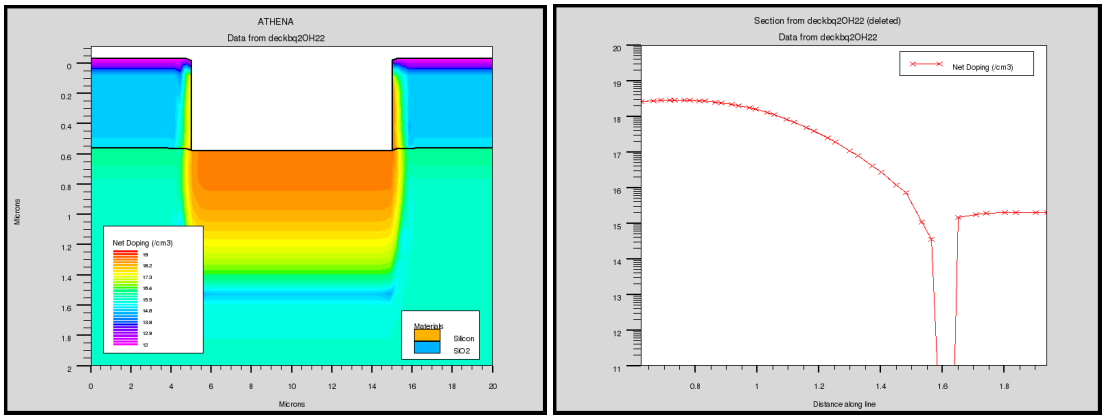

Figure 15 – Silvaco Athena simulations of a 10 µm wide p+ diffused resistor. 2D profile (left) and vertical cutline (right). Simulations predict a sheet resistance of 523 Ω/□.

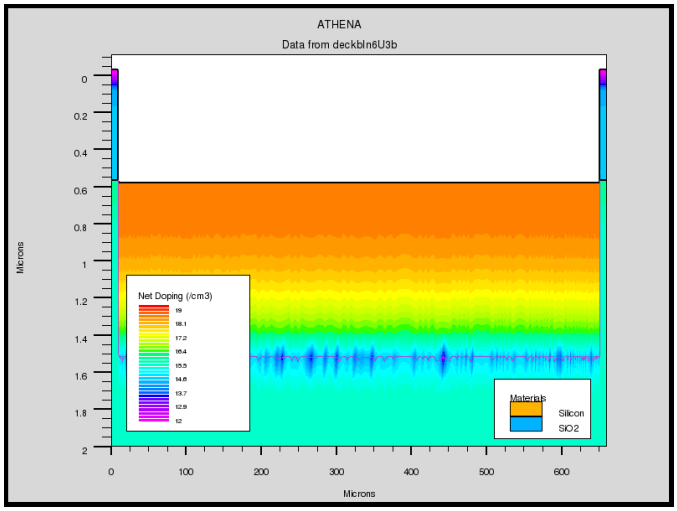

Figure 16 - Silvaco Athena simulations of a 640 µm wide p+ diffused resistor. Simulations predict a sheet resistance of 538 Ω/□.

Chapter 4

Design

4.1 Device Designs

Several device parameters are investigated, including physical dimensions, diaphragm thickness, additional proof mass, center of gravity, and piezoresistors material. Diaphragm thickness is controlled by the duration of the backside KOH etch, and verified with optical and scanning electron microscopy. Thinner diaphragms should lead to more sensitive devices at the expense of lower mechanical shock resistance. Additional mass glued to the existing silicon proof mass should make the device more sensitive while adding manufacturing complexity and removing design symmetries if the masses are not perfectly aligned. To maximize X and Y axis sensitivity it is important to maintain a large center of gravity, so masses should only be added to one side of the diaphragm. Finally, the piezoresistor material must be taken into account. On a separate 1-axis accelerometers being co-fabricated, two identical cantilever accelerometers designed with both n+ polysilicon and p+ silicon piezoresistors will be tested. Both materials may exhibit a large gauge factor due to the band structure changes induced by stress. This increase in gauge factor may be negated in the polysilicon resistor due to small crystal grain size and high doping concentrations, so a side by side comparison will be useful in determining which material works best.

A layout of the all of the chips combined onto one contact lithography mask is shown in Figure 17. Twelve unique 10x10 mm dice, including one-axis accelerometers, three-axis accelerometers, and test structures, are spread over the four-inch wafer. Each

wafer holds sixty total chips. Table 3 shows the colors of each layer for this layout along with all future layout figures.

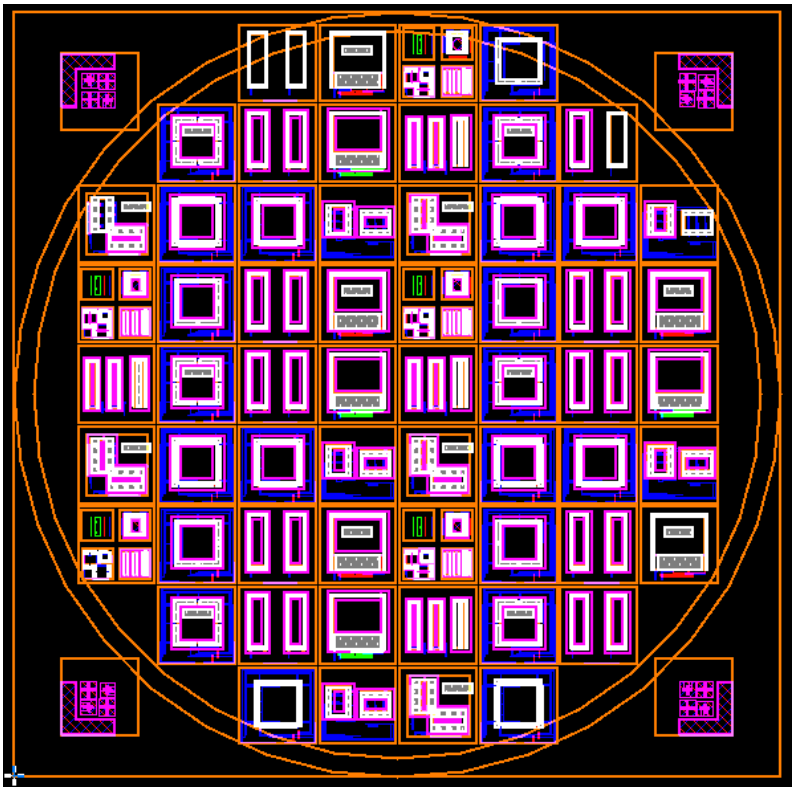

Figure 17 – 4" Contact alignment mask layout with all device designs and alignment marks.

P+ Silicon	Green
N+ Silicon	Orange
N+ Polysilicon	Red
Contact	Grey
Aluminum	Blue
Diaphragm	Purple
Top Hole	White

Table 3 – Schematic layers and colors

One of the twelve designs contains several test structures, shown in Figure 18. These structures are useful in calculating the sheet resistances of the substrate, p+ silicon, n+ polysilicon, and aluminum layers. Two p+ silicon layers of constant length and varying widths are used to measure the effects of lateral diffusion.

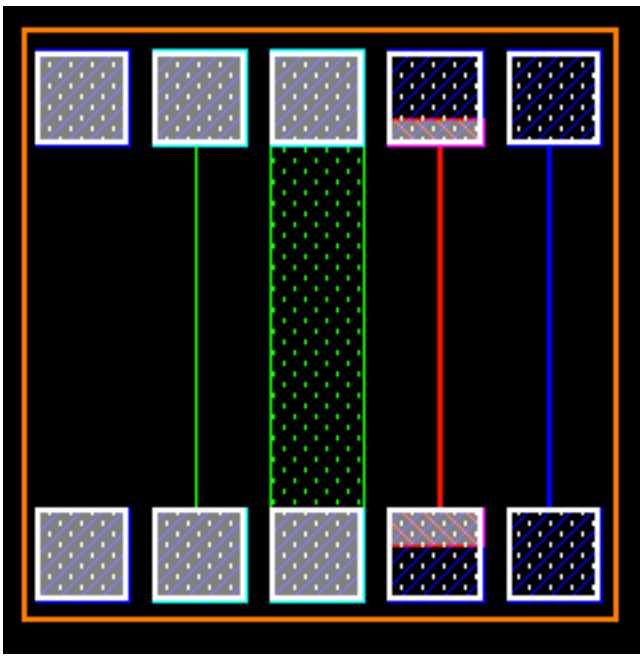

Figure 18 – 4x4 mm test structure. Includes connections over the n- substrate, p+ implant (narrow and wide), n+ polysilicon, and aluminum layers.

4.1.1 Dual Rectangular Structure

The first three-axis accelerometer design is shown in Figure 19, with additional wafer alignment marks in the upper right hand corner. Figure 20 shows the rectangular structures with Wheatstone bridge resistors overlaid on top of the model. Each of the six support beams is fixed to the bulk of the chip.

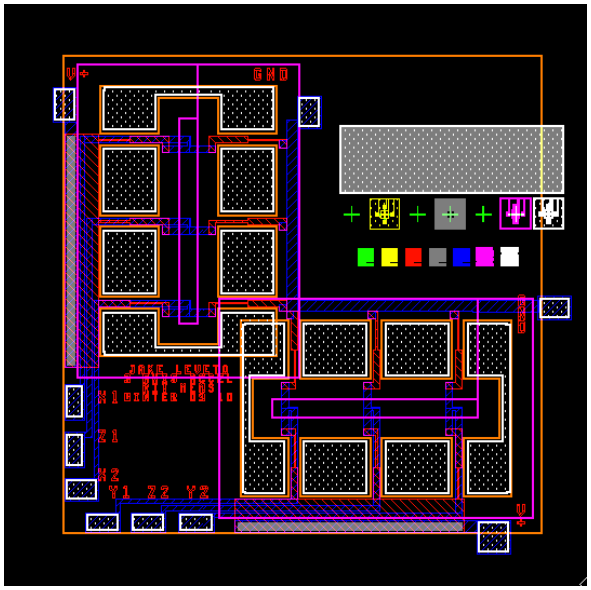

Figure 19 – Mask layout of the original dual rectangular structure, designed in the winter 2009-2010 quarter.

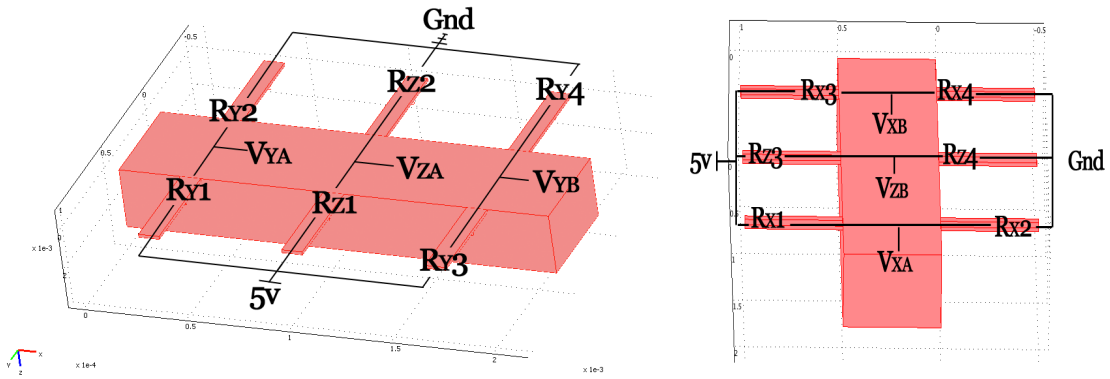

Figure 20 – Dual rectangular design with Wheatstone bridge resistor overlays

This design was the first and only design fabricated in the winter of 2009-2010, and two major design errors were encountered during testing. First, several of the contact pads overlap the diaphragm area, resulting in shattered dice during the wire bonding process. Second, the diaphragm area was drawn to aggressively so that the KOH removed too much of the silicon proof mass, dramatically lowering sensitivity. These two issues have been fixed, with the new design shown in Figure 21. In addition the metal lines and spaces in between are larger to improve yield, and the two rectangle structures were placed further apart to help reduce any cross talk between the two structures.

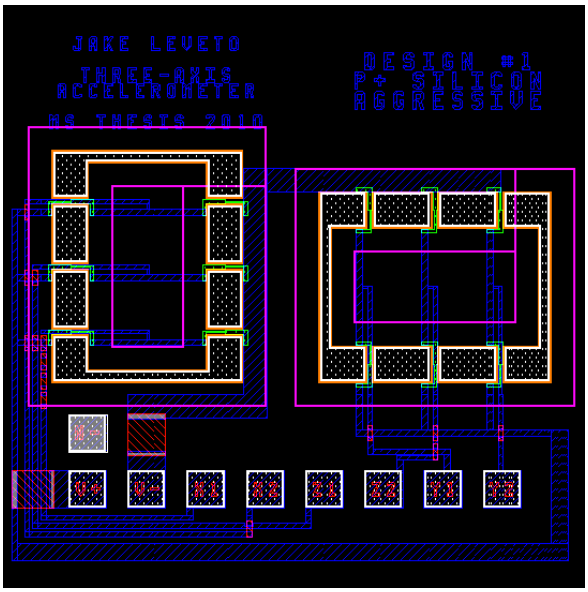

Figure 21 - Mask layout of the improved dual rectangular structure, designed in spring 2010.

4.1.2 Monolithic Structure #1

One possible improvement to the dual rectangular structure is to combine both structures into a single proof mass with only four support beams. This allows for more sensitive devices because of a larger mass to spring constant ratio. This could also be beneficial to chips with integrated electronics, as all of the devices can be placed on the single proof mass instead of two. The first structure designed, shown in Figure 22, has a single square proof mass with four short rectangular arms supporting it. The three Wheatstone bridges are shown in Figure 23, with the horizontal arms supporting the X and Z bridges and the vertical arms supporting the Y bridge.

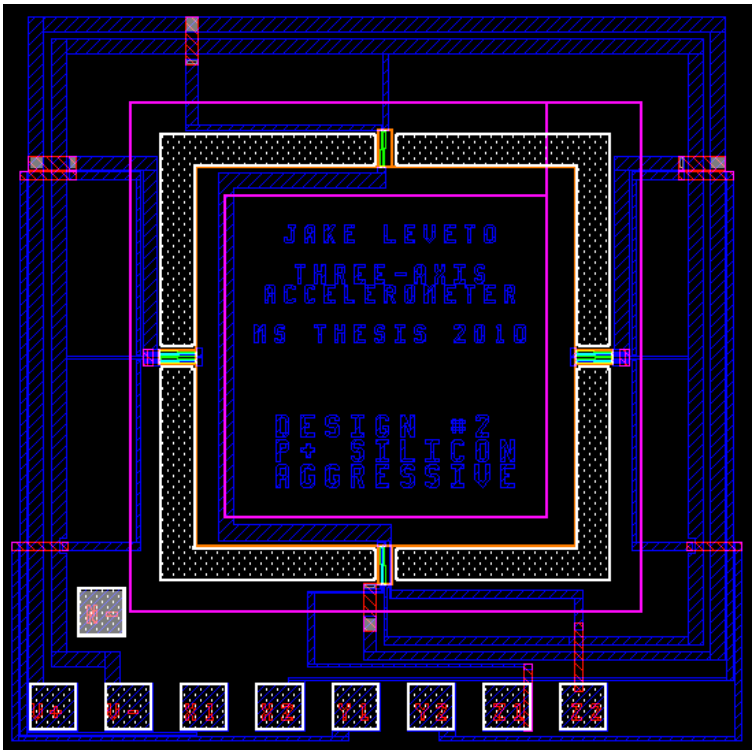

Figure 22 – Mask layout of the high sensitivity monolithic structure #1. A lower sensitivity version with wider support arms and polysilicon piezoresistors is also fabricated.

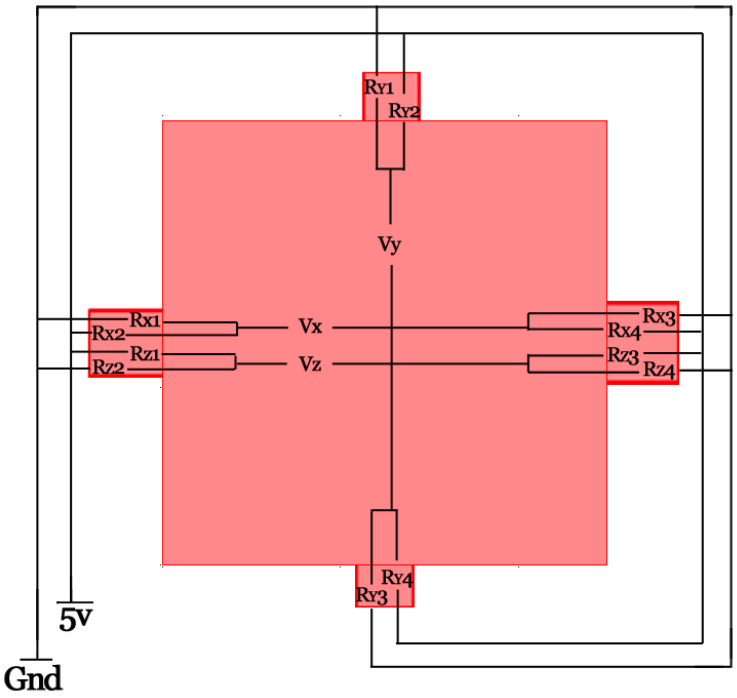

Figure 23 - Monolithic structure #1 with three Wheatstone bridges overlaid

4.1.3 Monolithic Structure #2

One possible improvement to increase sensitivity involves lowering the effective spring constant of the system by increasing the length to width ratio of the support beams. This is done in Figure 24, which is the same as Figure 22 with the exception of newly designed support arms. The Wheatstone bridges are almost identical, Figure 25 shows the resistors overlaid over the design.

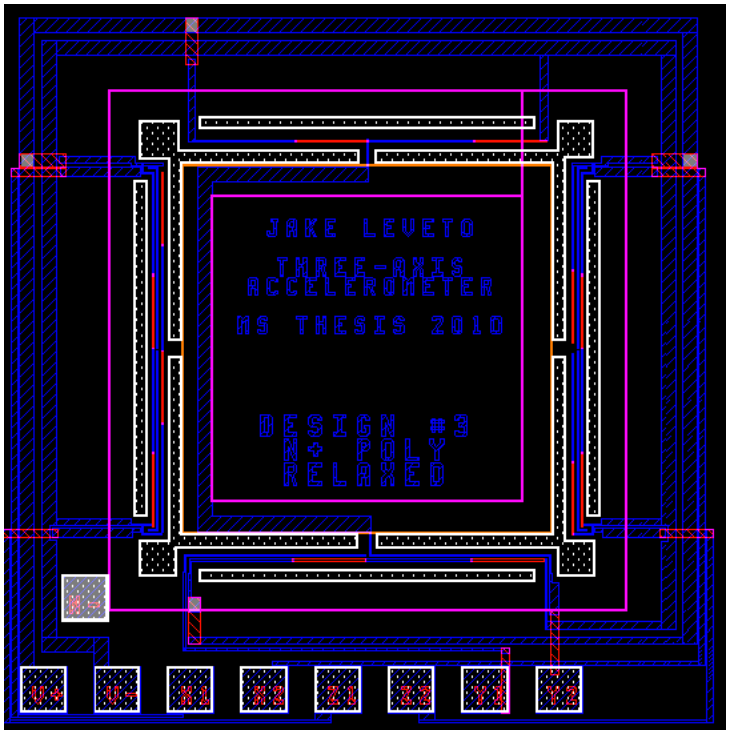

Figure 24 - Mask layout of the low sensitivity monolithic structure #2. A higher sensitivity version with more narrow support arms and p+ diffused piezoresistors is also fabricated.

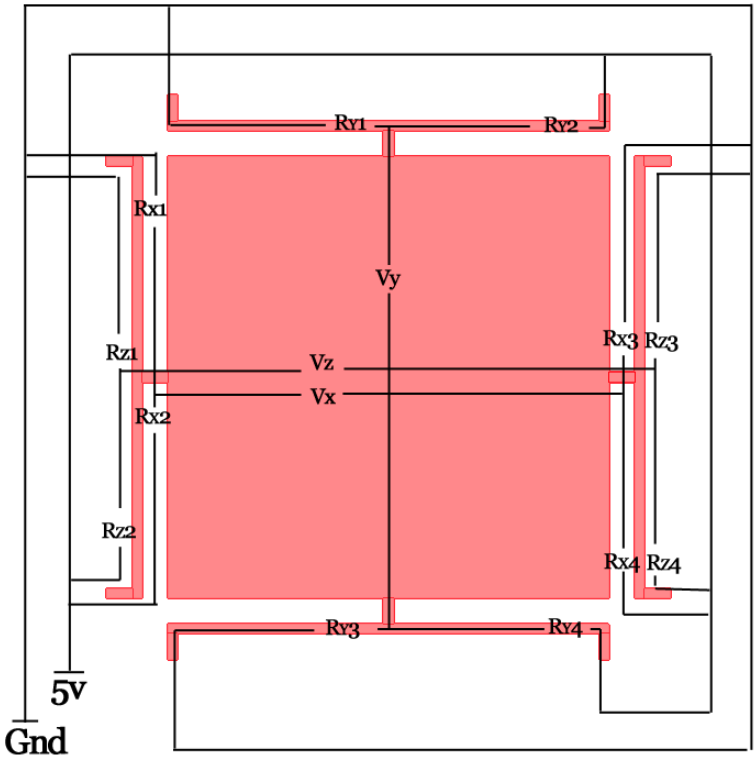

Figure 25 – Monolithic structure #2 with three Wheatstone bridges overlaid

4.2 Piezoresistor Bridge Configuration

All of the above designs are based on the principle that each of the three bridges outputs a voltage only when the correct direction of acceleration is applied. Figure 26 visually shows the change in each bridge when the correct direction of acceleration is applied. Table 4 and Table 5 show the response of each resistor in all three Wheatstone bridges when all three directions of acceleration are applied. While both tables are similar and give the same final results, there are a few subtle differences. Table 4 shows the response of the dual rectangular structure while Table 5 shows the response of both monolithic structures.

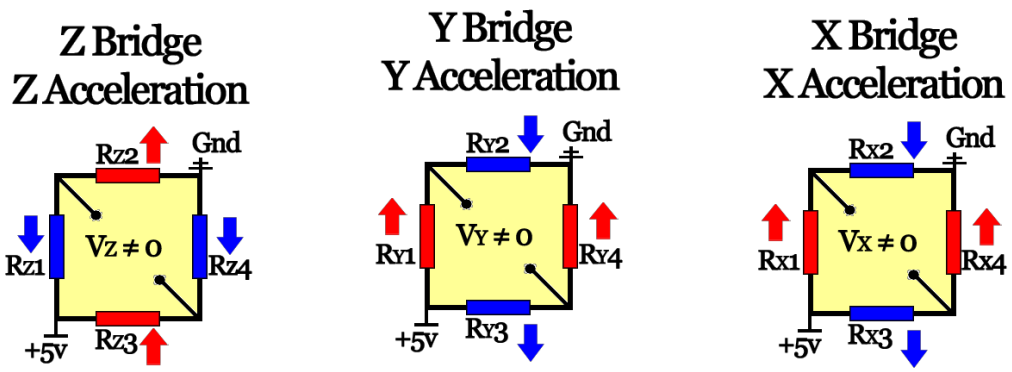

Figure 26 – Bridge configuration for all three axes. See Appendix 2 for the other acceleration conditions

	X Bridge					Y Bridge					Z Bridge				
Acceleration	Rx1	Rx2	Rx3	Rx4	ΔVx	Ry1	Ry2	Ry3	Ry4	ΔVy	Rz1	Rz2	Rz3	Rz4	ΔVz
X	+	-	-	+	+	0	0	0	0	0	0	0	-	-	0
Y	0	0	0	0	0	+	-	-	+	+	+	+	0	0	0
Z	-	-	+	+	0	-	-	+	+	0	-	+	+	-	+

Table 4 – Dual rectangular bridge resistor changes under X, Y, and Z acceleration.

	X Bridge					Y Bridge					Z Bridge				
Acceleration	Rx1	Rx2	Rx3	Rx4	ΔVx	Ry1	Ry2	Ry3	Ry4	ΔVy	Rz1	Rz2	Rz3	Rz4	ΔVz
X	+	-	-	+	+	0	0	0	0	0	+	+	-	-	0
Y	0	0	0	0	0	+	-	-	+	+	+	+	0	0	0
Z	-	-	+	+	0	-	-	+	+	0	-	+	+	-	+

Table 5 – Monolithic structure #1-2 bridge resistor changes under X, Y, and Z acceleration. Differences from Table 4 in Z bridge under X acceleration

4.3 Physical Dimensions, Materials, and Sensitivities

All of the physical dimensions of the accelerometers affect the total mass of the system, effective spring constant, and damping coefficient. These factors ultimately determine the sensitivities and resonant frequencies of the devices. Table 6 shows the characteristics of all six versions of the three-axis accelerometers. Variables include whether or not the resistor is made up of n+ polysilicon or p+ diffused silicon, along with support beam dimensions after lateral etching from fabrication. Piezoresistive coefficients

are estimated from the material type and doping levels, theoretical sensitivities are then calculated with the maximum strains from the FEA simulations.

Description	Resistor Type	Proof Mass [µm]	Supports [µm]	Piezo. Coefficient [Pa-1]	Z Strain [g-1]	Z Sens. [mV/gV]	XY Strain [g-1]	XY Sens. [mV/gV]
Dual Rect #1	Poly	3500 x 2000	540 x 180	1.18E-11	2.5E-06	0.005	4.0E-07	0.001
Dual Rect #2	p+	4200 x 1100	860 x 320	5.00E-10				
Monolithic #1	p+	5000 x 5000	420 x 280	5.00E-10	5.0E-06	0.425	1.2E-06	0.102
Monolithic #1	Poly	5000 x 5000	420 x 480	1.18E-11	2.5E-06	0.005	5.0E-07	0.001
Monolithic #2	p+	5000 x 5000	2600 x 160	5.00E-10	1.0E-04	8.500	1.6E-05	1.360
Monolithic #2	Poly	5000 x 5000	2600 x 320	1.18E-11				

Table 6 – Theoretical piezoresistive coefficients and sensitivities for the fabricated accelerometers. Unlisted sensitivities were not simulated and should be lower than the less aggressive versions.

While the monolithic #2 structure with p+ silicon shows a very high sensitivity of 85 mV/gV, it comes at a price. Table 7 shows that the resonant frequency of this device is 151 Hz, potentially limiting it to low frequency applications. The other devices have resonant frequencies from 3500 to 8200 Hz, more in the range of current commercial capacitive accelerometers.

Description	Proof Mass [µm]	Supports [µm]	Z Resonance [Hz]	XY Resonance [Hz]
Dual Rectangular #1	3500 x 2000	540 x 180	4067	8164
Dual Rectangular #2	4200 x 1100	860 x 320		
Monolithic Design #1	5000 x 5000	420 x 280	3582	4750
Monolithic Design #1	5000 x 5000	420 x 480		
Monolithic Design #2	5000 x 5000	2600 x 160	151	231
Monolithic Design #2	5000 x 5000	2600 x 320		

Table 7 – Device dimensions along with simulated resonant frequencies. Unlisted frequencies were not simulated but should be higher than the less aggressive versions.

4.4 Process Constraints

Mask designs are drafted in Mentor IC Station, where each mask layer is drawn exactly to scale. This is the same software used to design custom integrated circuits, and is more than capable of laying out MEMS devices. Because design rules have not been

defined for the MEMS fabrication process, detail must be paid to all aspects of the layout to ensure the finished chips operate correctly.

Figure 27 shows the cross section of a finished MEMS device using the RIT bulk MEMS process. Etch undercutting must be taken into account for both the backside KOH and top hole etches. KOH etches along the (100) crystal plane, forming an angle of 54.74° with the back of the wafer. With a 525 µm thick wafer the diaphragm must be drawn 352 µm larger. The top hole is created with an isotropic silicon etch, so the top hole must be drawn 30 µm smaller than the finished design.

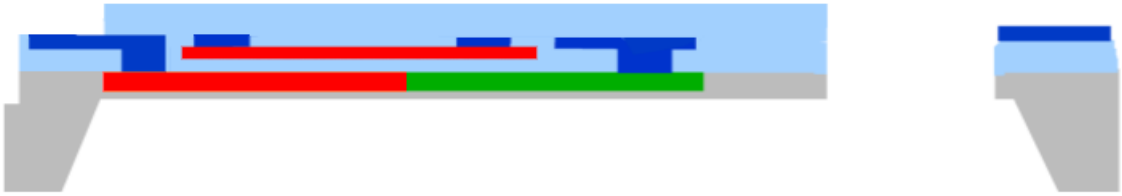

Figure 27 – Cross-section after RIT bulk MEMS processing [2]

Chapter 5

Fabrication

5.1 Bulk MEMS Process Flow

Fabrication was completed at the Semiconductor and Microsystems Fabrication Laboratory (SMFL), located at RIT. Processing was initially done along with the winter MEMS class using Fuller's bulk micromachining process [2]. This process includes a backside KOH diaphragm etch and front side top hole. In addition, it includes both n+ and p+ diffusion layers with one layer of n+ polysilicon and aluminum. Due to the relatively large features and the goal of low manufacturing costs, contact lithography was used with conservative design rules of λ = 10 μm.

Full process details are listed in **Error! Reference source not found.**, and Figure 27 shows a cross-section of what a finished device should look like. Figure 28 through Figure 39, drawn by Ivan Puchades, show cross sections of the device at various points throughout the process [30].

The RIT bulk MEMS process starts with 4" n-type <100> wafers. The wafers are initially thinned from 525±25 μm down to 300 μm using a wafer grinding tool, followed by Chemical Mechanical Planarization (CMP) for a mirror surface on both the front and back side of the wafer. This mirror finish is needed for the backside KOH etch later in the process. After a decontamination and RCA clean, 5000 Å of SiO_2 is grown at 1100° C. This oxide is then patterned with the first photolithography step and etched in Buffered Oxide Etch (BOE). Borofilm 100 is then spun onto the wafer, shown in Figure 29 (not to scale).

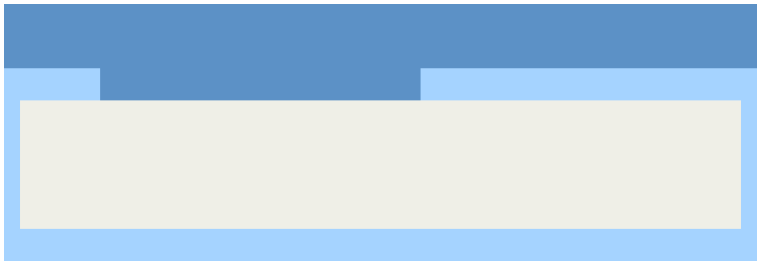

Figure 28 – RIT Bulk MEMS Process – Ready for p+ diffusion

Next the wafers are put into a diffusion furnace to dope the exposed areas with boron. During the last portion of the diffusion step, water vapor is introduced to grow an additional 1000 Å of oxide over the exposed areas. This creates a topographical step that is used to align all future photolithography layers. Once the diffusion step is complete, all of the Borofilm and existing oxide is etched away using BOE. The same steps are then repeated to dope the n+ region with phosphorus, and afterwards the wafers look like Figure 29.

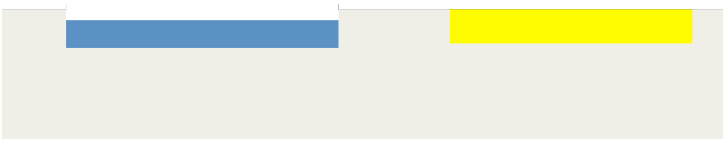

Figure 29 – RIT Bulk MEMS Process – After n+ diffusion

After all surface doping is completed, a 500 Å stress relief oxide layer is grown followed by a 1500 Å Low Pressure Chemical Vapor Deposition (LPCVD) of Si_3N_4. This nitride will be used in the future to protect select areas on the back of the wafer from KOH. The nitride on the front of the wafer is removed by protecting the back and sides of the wafer with photoresist, then plasma etching the nitride and wet etching the pad oxide. Next the photoresist can be removed, and after a RCA clean a 5000 Å layer of thermal oxide can be grown on the front of the wafer to act as an ILD (Inter Level Dielectric). The wafer progress is now shown in Figure 30.

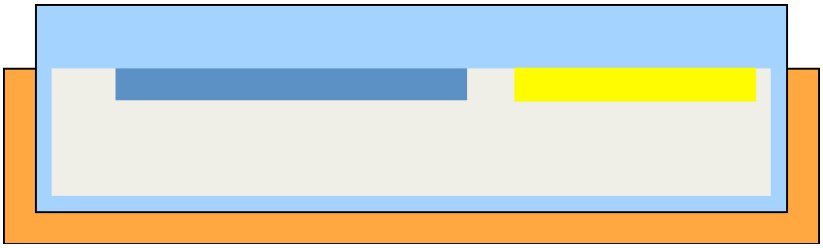

Figure 30 – RIT Bulk MEMS Process – Backside nitride deposited

The backside diaphragm photolithography step requires additional work since the Karl Suss 150A contact aligner only supports front side alignment. After coating the backside of the wafer with photoresist, a single drop of water is placed on the front of the wafer and the photo-1 mask is aligned as usual. When contact is made from the photo-1 mask to the wafer, the water acts as temporary glue and holds the wafer and mask together. The pair can then be flipped over, where the diaphragm mask can manually be aligned to the photo-1 mask. Once aligned, the two masks are clamped together. Finally, the backside is exposed under the Karl Suss, with the results shown in Figure 31.

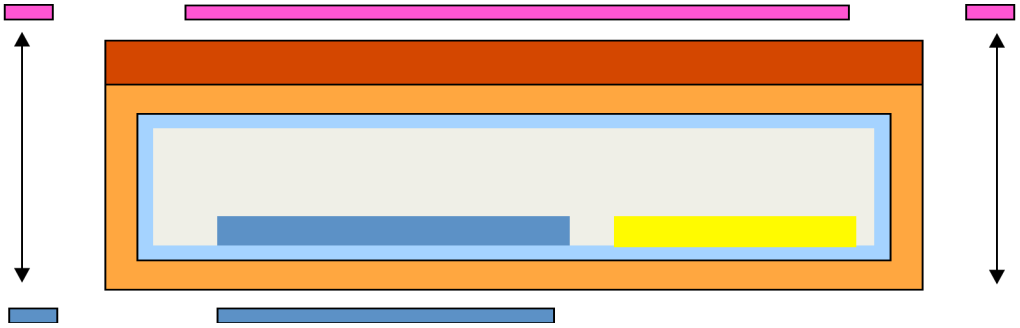

Figure 31 – RIT Bulk MEMS Process – Backside alignment

Once the photoresist is developed, the front and side of the wafer must be protected with photoresist so that the back can be etched. This etch consists of a BOE oxynitride etched, followed by a plasma nitride etch, finished with a final BOE pad oxide etch. Before the patterned resist is stripped the wafers look like Figure 32.

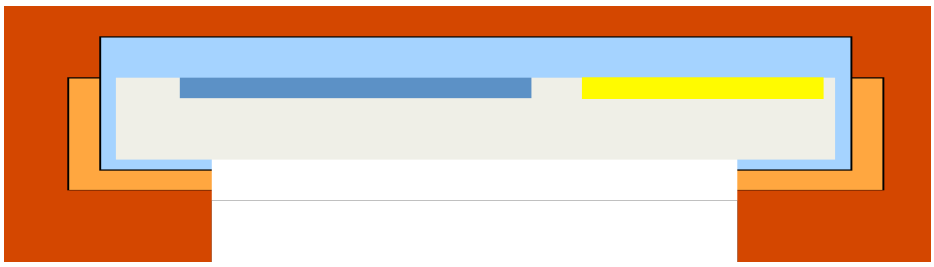

Figure 32 – RIT Bulk MEMS Process – Diaphragm hard mask etched

Next, 6,000 Å of polysilicon is deposited in the LPCVD tool. This puts down un-doped small grain polysilicon, which is then doped using phosphorus spin on glass in the furnace. After etching the spin on glass off of the polysilicon, the wafers look like Figure 33.

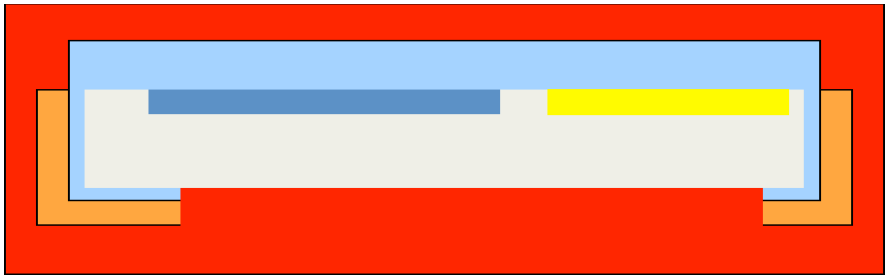

Figure 33 – RIT Bulk MEMS Process – Doped polysilicon deposited

After the polysilicon is deposited and doped, it is then patterned and the front is side plasma etched. The polysilicon is left on the back of the wafer to protect the nitride diaphragm hard mask, and will be removed later in the process. 10,000 Å of Low Temperature Oxide (LTO) is then deposited on the front and back of the wafer in the LPCVD tool. This layer of oxide serves as the second ILD on the front, and will later be removed on the back. The wafer is now shown in Figure 34.

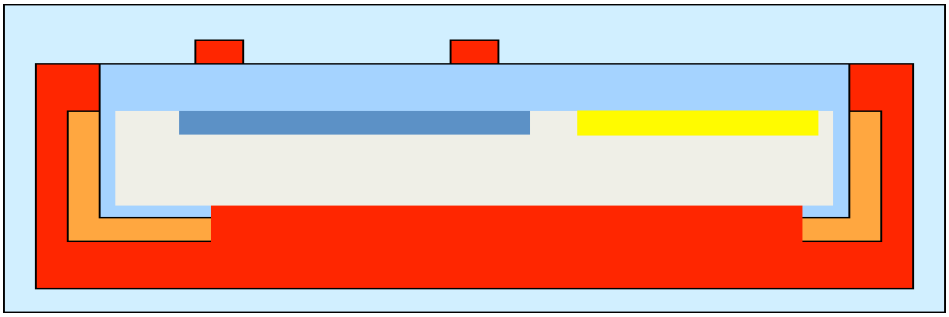

Figure 34 – RIT Bulk MEMS Process – ILD2 deposited

Contacts are then wet etched to both the polysilicon and silicon surfaces. After contacts are made, and an RCA clean is performed, the first layer of metal is deposited. A 10,000Å layer of aluminum is sputtered onto the front of the wafer and into the contact cuts, shown in Figure 35.

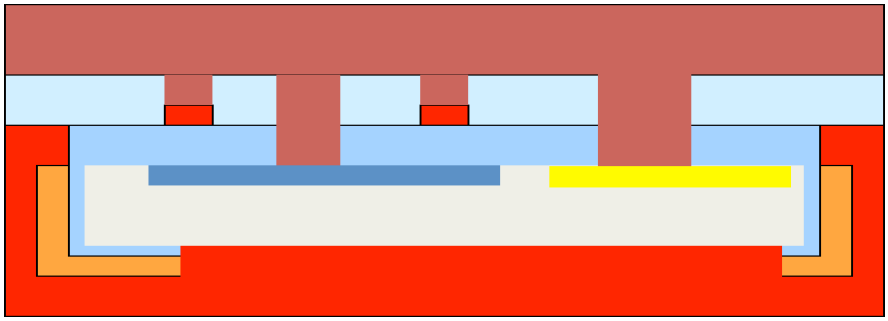

Figure 35 – RIT Bulk MEMS Process – Metal1 deposited

The first layer of metal is then patterned using an aluminum wet etched. A third ILD of 10,000Å LTO is then deposited onto both sides of the wafer using the LPCVD tool. A second layer of aluminum is then sputtered onto the front of the wafer, now shown in Figure 36. This second layer of metal is not used for electrical purposes, but as a hard mask to the future top hole silicon etch.

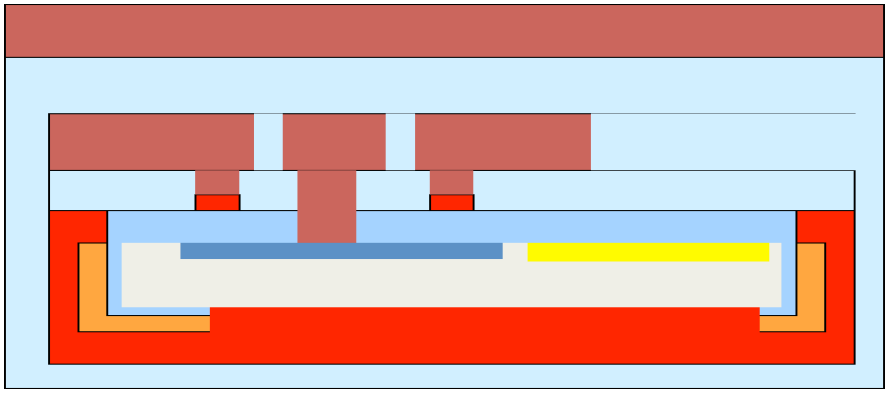

Figure 36 – RIT Bulk MEMS Process – Metal 2 deposited

The second layer of aluminum is patterned and etched in the same way as the first layer. Next a final layer of LTO is deposited to promote adhesion of the forthcoming PROTek layer. PROTek is a spin on plastic used to protect the front of the wafer from hot KOH. The PROTek is spun coat at 1500 RMP, followed by a 200° C bake for 20 minutes. Next the diaphragm is etched into the backside of the wafer. First the LTO on the back of the wafer is etched away with BOE. The wafers are then placed in a 75° C KOH bath, which etches the protecting polysilicon layer and then into the bulk silicon. KOH Etches along the <111> silicon plane, so on a <100> wafer this makes a 54.74° angle, as shown in the bottom of Figure 37. Since there is no etch stop for the KOH, the etch depth and etch rate must be measured and calculated half way through the etch step. Using this etch rate along with the wafer thickness, current etch depth, and desired diaphragm thickness, the remaining etch time can be calculated. The wafers now look like Figure 38.

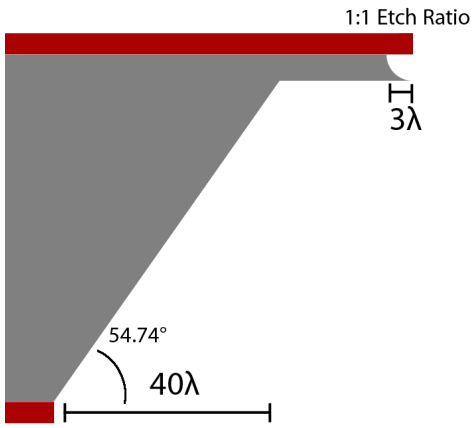

Figure 37 – Lateral KOH etch (bottom) and Reactive Ion Etch (RIE) (top). λ = 10 µm, diaphragm thickness = 30 µm.

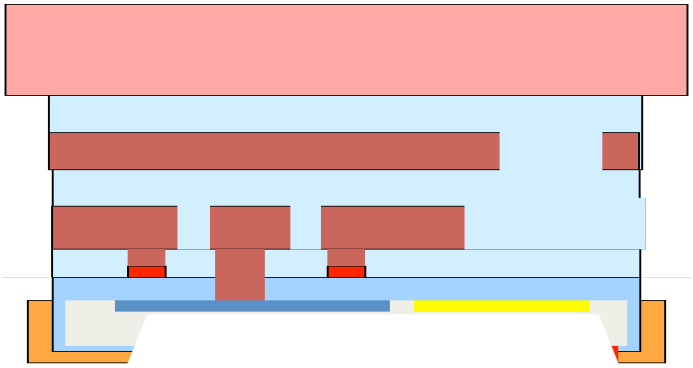

Figure 38 – RIT Bulk MEMS Process – Diaphragm etched

After the diaphragm is complete, the PROTek layer is removed using a special solvent stripper. PROTek often sticks to the substrate, so an O_2 plasma etch, also known as photoresist ash, can be used to remove any remaining PROTek. Next, the adhesion promotion oxide layer must be removed with pad etch. Pad etch is used because normal HF and BOE attack aluminum, while pad etch is more selective to the underlying aluminum layer. This etch step also goes through any oxide not protected by the top aluminum layer, exposing the silicon surface in select areas.

At this point the wafers must be diced into individual die before further processing. This inconvenience is necessary because the wafers will be too brittle to dice after the top hole etch. After the wafers are diced they go through the SF_6 plasma top hole etch. This etches all way through the silicon diaphragm wherever the second layer of aluminum is not present, releasing the devices. The last step is to then remove the second metal layer and the underlying ILD using wet chemistry. The finished devices, shown in Figure 39, are now ready to be wire bonded and tested.

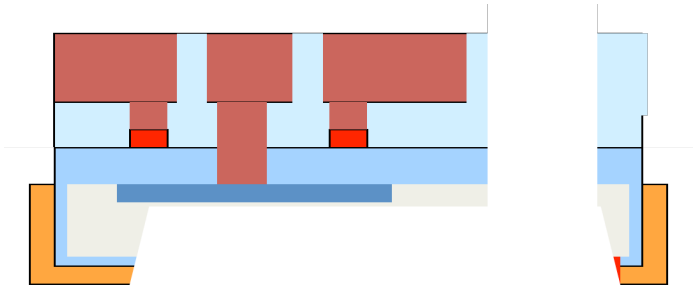

Figure 39 – RIT Bulk MEMS Process – Finished devices

The RIT bulk MEMS process was completed twice for this project. The first time the chips were fabricated along with the winter 2009-2010 MEMS class, and included the first iteration of the dual rectangular structure in from Figure 11. The second batch was performed from March until May 2010, and used a slightly different process. Differences in the spring process include ion implant p+ and n+ regions, omission of the wafer grinding step, and using TEOS from the P5000 Plasma Enhanced Chemical Vapor Deposition (PECVD) tool instead of LTO on some of the later IDL steps.

5.2 Processing Issues

Several issues were encountered during processing, which ultimately led to the failure of all devices. These processing issues must be resolved before new devices are fabricated to ensure that the same problems won't resurface. Issues encountered include poor aluminum step coverage, diaphragm etch protection layer delamination, and pad etch attacking aluminum.

The CVC 601 magnetron-sputtering tool was used to deposit all aluminum layers. This is a form of Physical Vapor Deposition (PVD) where energetic argon ions bombard an aluminum target, dislodging aluminum atoms, which are then collected onto the surface of the substrate. This form of deposition is capable of depositing a uniform layer onto flat topology, but issues arise when trying to uniformly cover large and steep topography steps. In the RIT bulk MEMS process, the 10,000 Å metal-1 layer of aluminum must cover a via step of 5,000 Å and a polysilicon step of 6,000 Å. Figure 40 shows images of the poor aluminum coverage over polysilicon and into a contact via on one of the finished devices. The voids are present throughout the entire die and wafer, causing all finished circuits to test open.

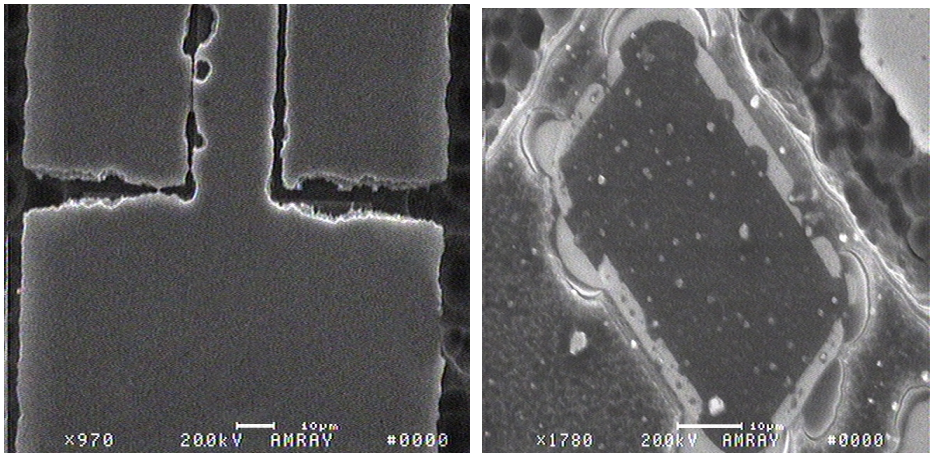

Figure 40 – Secondary Electron Micrograph (SEM) of poor aluminum step coverage over polysilicon lines (left) and into a contact via (right).

Several solutions exist to remedy this issue. The simplest solution is to make the aluminum film thick relative to the steps so that the aluminum completely covers any topography. This is analogous to a large snowstorm completely covering a staircase, once enough snow accumulates all topography over the stairs is smoothed over. Problems with this method do exist, so it is not always a viable solution. First, highly stressed materials will eventually hit a critical stress level, causing defects in the film. Second, this method is not sustainable for designs with many layers of metal. The films would need to be continually thicker, eventually causing issues with high aspect ratios features and deposition tool throughput.

Another possible solution includes the use of substrate heating during deposition, which has been shown in Figure 41 to improve aluminum step coverage [31]. This is due to surface atoms mobility at elevated temperatures. For aluminum, the substrate must be heated to at least 250 °C to see any noticeable effects. One drawback of heating the substrate is that the average grain size of the deposited film increases. This causes the aluminum to look hazy, often creating difficulty in photolithography alignment and causing poor photoresist adhesion due to increased surface roughness.

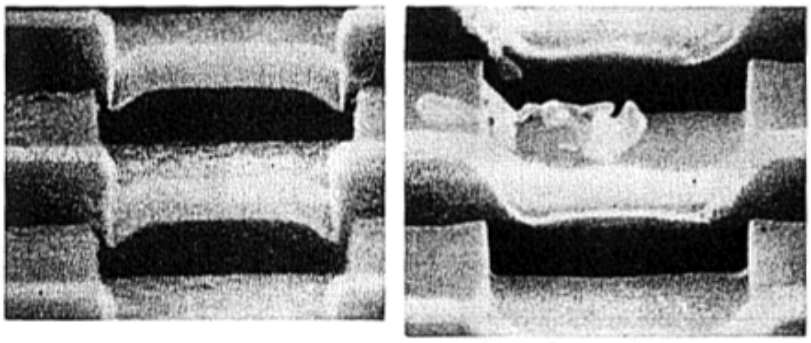

Figure 41 – Aluminum step coverage without (left) and with (right) a heated substrate [31]

A partially heated sputter was used on the final wafer processed during the second fabrication run. Ten minutes before deposition a heat lamp was turned on and set to 300 °C. The first two minutes of deposition was done with the heat lamp on, while the remaining 30 minutes were finished with the lamp off to reduce surface roughness. Testing after the following photolithography and aluminum etch steps showed that all circuits were complete and that the aluminum step coverage issue has been resolved.

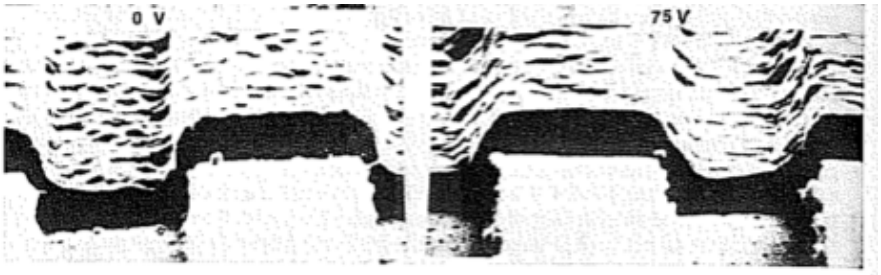

Figure 42 – Aluminum step coverage without (left) and with (right) a 75V RF bias sputter [31]

Another potential solution to the step coverage issue includes the use of bias sputtering. In this technique, a RF bias is applied to the wafer during deposition. This causes the wafer to acquire a negative self-bias, which accelerates ions towards the surface. These ions then collide with the deposited film, ejecting atoms from the surface

onto any near sidewalls. Aluminum could also be deposited with other techniques such as Metal Organic Chemical Vapor Deposition (MOCVD) and Atomic Layer Deposition (ALD). Finally, CMP could be used to flatten all topography before metal deposition.

Another issue encountered during processing involved the front surface protection layer during the backside diaphragm KOH etch. Brewer Science's ProTek B3 coating was used to protect the front surface for 6-8 hours in the 75° C KOH bath [32]. Even with an adhesion promoting oxide layer and a surface treatment before applying the ProTek, the etched wafers showed signs of surface damage in areas where the protection layer delaminated. This issue was more present on the wafer that was continually measured for etch depth, indicating that each cycle in and out of the KOH induces more defects. One possible cause is that the bottle of ProTek B3 used expired over three years ago, sometime in 2007. Using a new unexpired bottle may help stop delaminating, reducing front surface damage.

In addition to using new ProTek, the use of an etch stop layer could also improve this process step. KOH is known to etch both p+ silicon and silicon dioxide hundreds to thousands of times slower than lightly doped silicon [24]. The use of an etch stop would allow for the wafers to remain submerged in KOH from the start until the end of the etch, reducing defects associated with rinsing, measuring, and reintroducing the wafer to KOH. The addition of an etch stop is unlikely to be viable for this design, as the ideal diaphragm thickness for the accelerometers is much thicker than the etch stop could support through the use of either a p+ ion implantation or Silicon On Insulator (SOI) substrates.

One final issue encountered while processing was pad etch attacking the aluminum metal-1 lines after the overlying oxide had been fully etched. Pad etch is a combination of 5 parts Buffered Oxide Etch (BOE) and three parts glycerin, and is used to etch on top of aluminum. Hydrofluoric Acid (HF) and BOE are known to attack aluminum as well as oxide, but the glycerin in the pad etch helps protect the aluminum. While pad etch is significantly better than BOE or HF, it still attacks aluminum at a slower rate. It is believed that while etching the oxide over the metal-1 layer, the pad etch eventually attacked the aluminum lines. This caused open circuits at the weakest points in the devices, where the aluminum crosses polysilicon lines and goes into contact vias. Micrographs of the final wafer, the one with the heated aluminum sputter, look similar to those in Figure 40.

Two relatively simple solutions exist to fix this problem. Pad etch can still be used, but care must be taken to prevent the aluminum from etching after the oxide is cleared. Step coverage of the aluminum must be further improved, and the etching of the oxide over aluminum must be more precise. Different oxides types and different temperatures cause different etch rates, so the exact etch rate and time must be calculated for the specific oxide layer being etched. This could be done using a dummy wafer to measure the initial oxide thickness and etch rate.

An alternate solution is to replace the wet pad etch step with a dry plasma oxide etch. Silicon dioxide is typically etched in a fluorine-based gas such as SF_6, while aluminum is typically etched with a chlorine-based gas such as Cl_2 [33]. This allows for the oxide to be selectively etched, leaving the underlying aluminum untouched. Plasma

etching also has several other advantages, such as being able to etch into smaller features and allowing for higher aspect ratios.

5.3 Finished Devices

Figure 43 shows two completed three-axis accelerometers, each composed of several micrographs stitched together using image editing software. Appendix 4 shows a high-resolution image of the monolithic #2 design, zoomed in to show the three resistor bridges. In addition to the three-axis accelerometers, Figure 44 shows two of the one-axis accelerometers fabricated on the same wafers. The black areas show the top hole thru-etch, and the white lines represent both aluminum and polysilicon. The diaphragm, p+ diffused, and n+ diffused layers are not visible on the micrographs. The speckles present on all of the images are ProTek residue, which can be totally removed with an O_2 plasma etch.

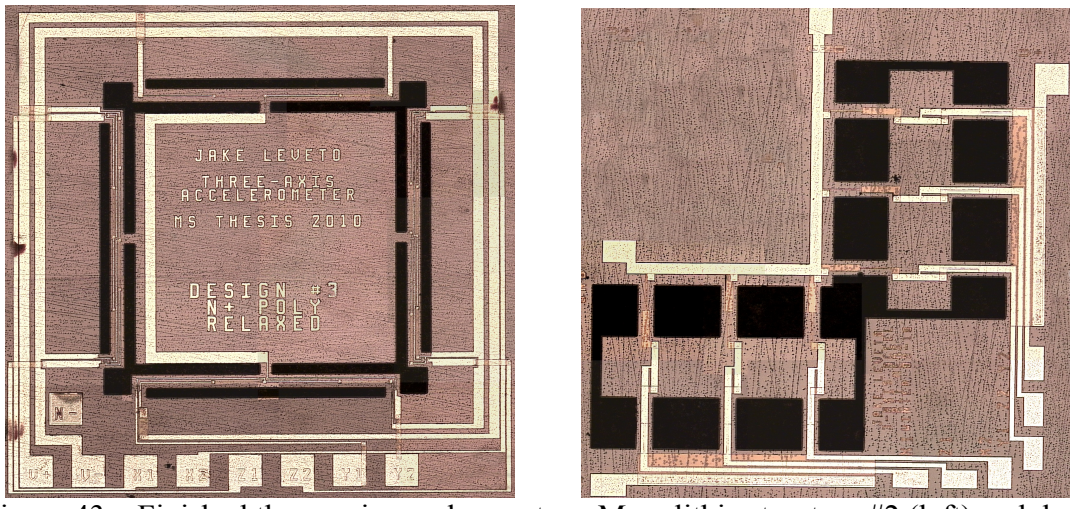

Figure 43 – Finished three-axis accelerometers. Monolithic structure #2 (left) and dual rectangular structure (right). The black area represents the top hole release etch.

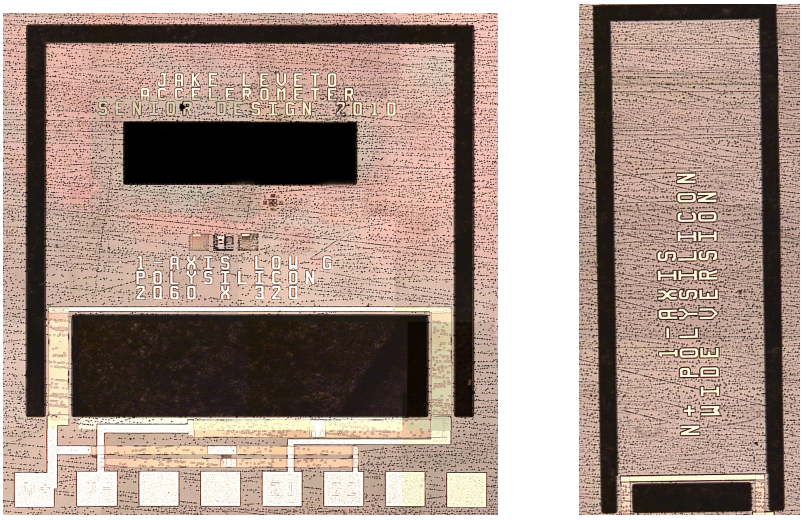

Figure 44 – One-axis accelerometers also fabricated on the same wafers.

Chapter 6

Testing

6.1 Introduction

Because of the aluminum step coverage and pad etch issues mentioned in Chapter 5, none of the finished chips yielded working devices. Instead of testing the designed accelerometers as proposed in the project proposal, commercial accelerometers were instead tested. Table 8 shows a list of the investigated accelerometers, also pictured in Figure 45. The ST Microelectronics LIS331DL is the current accelerometer in the Apple iPhone 3GS smart phone, and was interfaced with the AccelPlot application from Innovative Applications [34]. The Analog Devices ADXL30 accelerometer is currently used in the Nintendo Wiimote controller, and was interfaced using a Bluetooth connection and the open source DarWiinRemote application [35]. Both of these accelerometers are low-g and record digital signals with sample rates up to 100 Hz.

Company	Name	Type	Packaging	Axes
Analog Devices	ADXL30	Capacitive	Nintendo Wiimote	3
ST Microelectronics	LIS331DL	Capacitive	Apple iPhone	3
Analog Devices	ADXL278	Capacitive	SMD	2
Measurement Specialties	Minisense 100	Piezoelectric	Packaged	1
Analog Devices	ADXL330	Capacitive	SMD	3
Bosch	BMA 140	Capacitive	SMD	3

Table 8 – Tested accelerometers

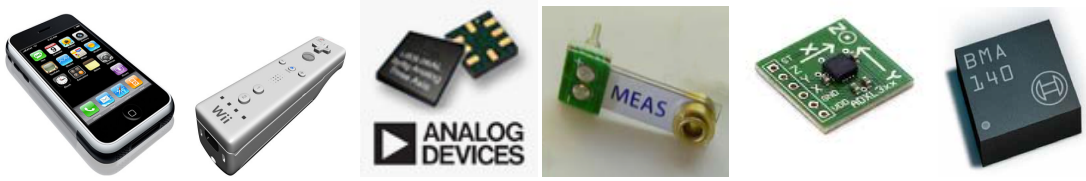

Figure 45 - Tested Accelerometer, listed from left to right, ADXL30 in the iPhone, LIS331DL in the Wiimote, ADXL278, Minisense 100, ADXL330, and BMA 140.

Two analog voltage output accelerometers were also investigated. The Analog Devices ADXL278 device is a two-axis high-g accelerometer capable of detecting ±70 g. The Measurement Specialties Minisense 100 is a one-axis piezoelectric high-g accelerometer that generates its own output voltage. This is beneficial in that it requires no power supply, but detrimental in that it is incapable of measuring steady state acceleration of frequencies below one Hertz.

The Analog Devices ADXL330 and Bosch BMA 140 sensors are low-g 3-axis accelerometers with analog voltage outputs. Because the digital 3-axis accelerometers and analog one and two-axis accelerometers were successfully tested, duplicate tests on these two backup accelerometers were not performed.

6.2 Methods

In preparation for the finished chip, Printed Circuit Boards (PCBs) have been designed and fabricated. Copper contact pads must be located near the correct chip pads so that wire bond connections can be made. Since the finished chip involves moving silicon parts, a 7x7 mm hole was drilled through the PCB area where the finished chip is placed. Since the accelerometer must be amplified in order to measure a strong signal, the PCB connecting pins are setup in a way to easily connect to the amplifier

Once the chip is connected to the PCB and wire bonded, testing can begin. Several techniques are used to measure acceleration and compare it to both theoretical models and existing commercial accelerometers. The simplest measurement technique involves the use of a cantilever beam, shown in Figure 46. Equation 10 shows the resonant frequency of the cantilever (f_o), where E is the Young's modulus, I is the moment of inertia, L is the length, and m is the mass of the cantilever. Equation 11 then

gives the acceleration, where $Y_{initial}$ is the initial deflection at the end of the cantilever. The two cantilever beams test structures at RIT are capable of outputting up to 15 and 100 g of acceleration.

$$f_o = \frac{1}{2}\pi\sqrt{\frac{3EI}{L^3 m}} \tag{10}$$

$$A = Y_{initial}(2\pi f_o)^2 \tag{11}$$

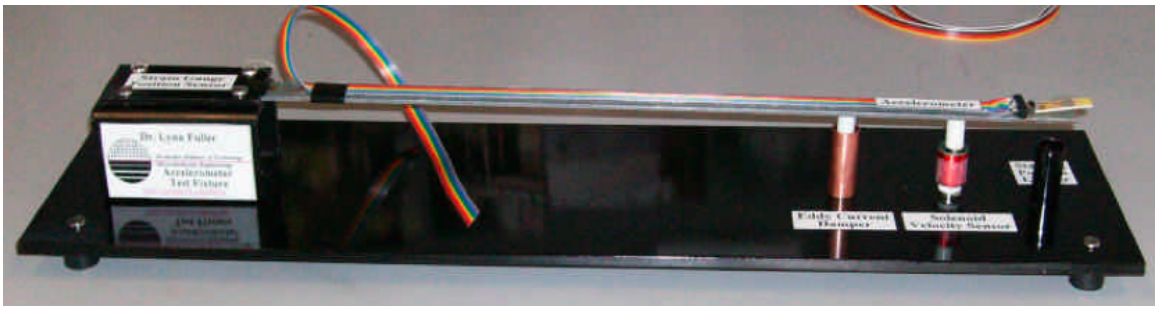

Figure 46 – Low g accelerometer testing units [6].

Another way to generate acceleration is to use an amplified audio speaker, shown in Figure 47. Driving the speaker with a sine wave in the form of Equation 12 leads to an equation for velocity and acceleration given by Equations 13-14, where Y is current displacement, Y_{max} is maximum displacement, ω is the frequency in radians per second, t is time, V is velocity, and A is acceleration. Placing a ruler near the speaker and taking a long exposure photograph while driving the speaker at a known frequency, shown in Figure 48, can measure the maximum displacement used to calculate maximum acceleration.

$$Y(t) = Y_{\max} \sin(\omega t) \tag{12}$$

$$V(t) = \frac{dY}{dt} = Y_{\max} \omega \cos(\omega t) \tag{13}$$

$$A(t) = \frac{d^2Y}{dt^2} = -Y_{\max} \omega^2 \sin(\omega t) \tag{14}$$

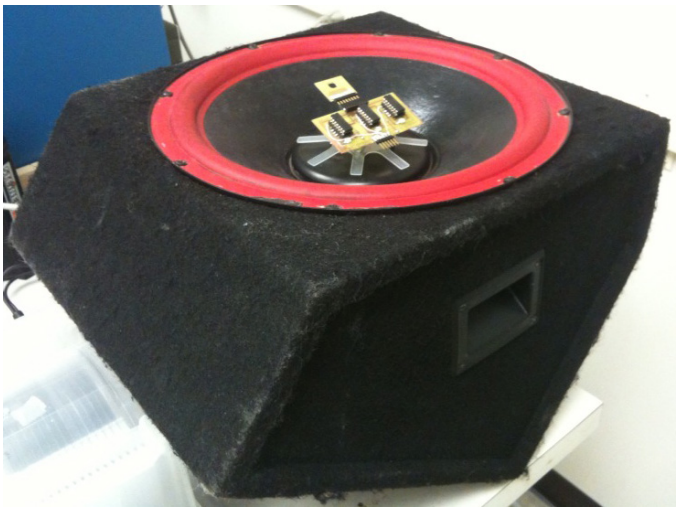

Figure 47 – Speaker accelerometer testing unit

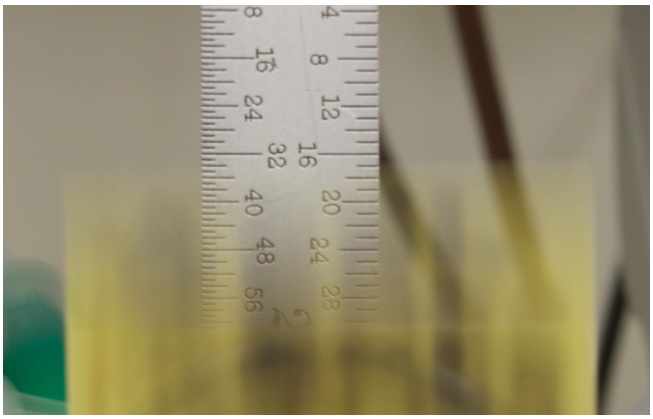

Figure 48 – Measuring maximum displacement of the speaker to calculate theoretical acceleration

An alternative to using an audio speaker driven by an amplifier is to use a Permanent Magnet Shaker (PM-Shaker). Figure 49 shows a commercial shaker that operates on the same electromagnetic principles as a speaker, and is capable of outputting up to 500 lbs of sinusoidal force.

Figure 49 – Permanent Magnet Shaker

The most basic measure of cross-axis sensitivity involves rotating the accelerometer 360° around each axis. While rotating around the x-axis, acceleration in the y and z directions are also measured. Theoretically, acceleration in the y direction should be at a maximum when acceleration in the z direction equals zero. This method may prove ineffective if the device is sensitive to only high accelerations, and typically requires a sensitivity of 0.001g [36]. Figure 50 shows the test setup and possible results. The two sinusoidal waves show both y and z acceleration, while the noise represents possible cross talk from the X-axis.

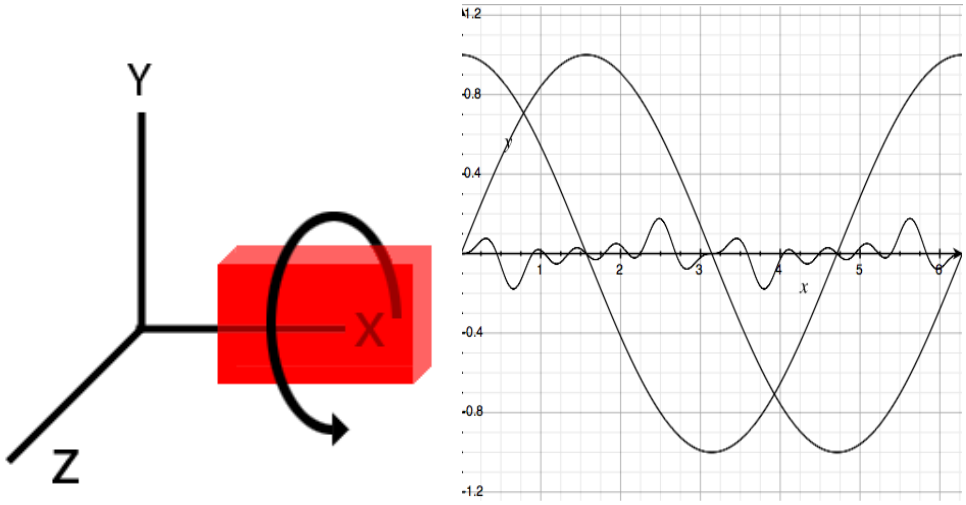

Figure 50 – Rotation test around the x-axis and sample results. The two sine waves show Y and Z acceleration while noise shows possible X acceleration due to axis cross talk

A better method to test cross-axis sensitivity involves using two orthogonal PM-Shakers, as shown in Figure 51. The shakers must be configured so that they are rotated exactly 90° from each other, and aligned horizontally so that there is no z component of acceleration. The shakers can them oscillate independently in the x and y direction. By shaking 90° out of phase circular motion can be achieved.

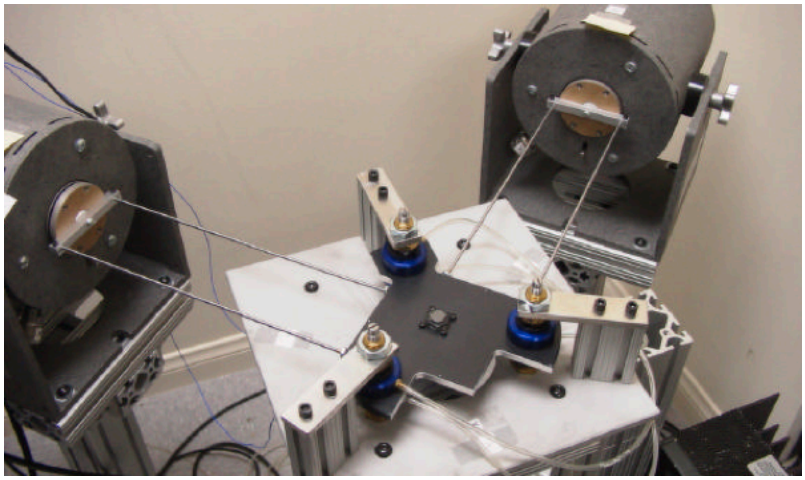
Figure 51 – Two orthogonal PM-Shakers for cross-axis sensitivity measurement [36]

The linearity of acceleration can be measured by comparing output voltage to known accelerations. This can be accomplished by either using a calibrated acceleration

source, or by using a commercial accelerometer reference that is known to be highly linear. Alternately, linearity can be measured using a cantilever and highly linear velocity sensor. If the accelerometer is truly linear, velocity should be out of phase with acceleration by 90° and proportionally related by a constant factor. If the proportionality factor varies as testing begins to damp and comes to a rest, than the accelerometer is not linear. Figure 52 shows two possible theoretical examples of non-linearity using the previously described methods.

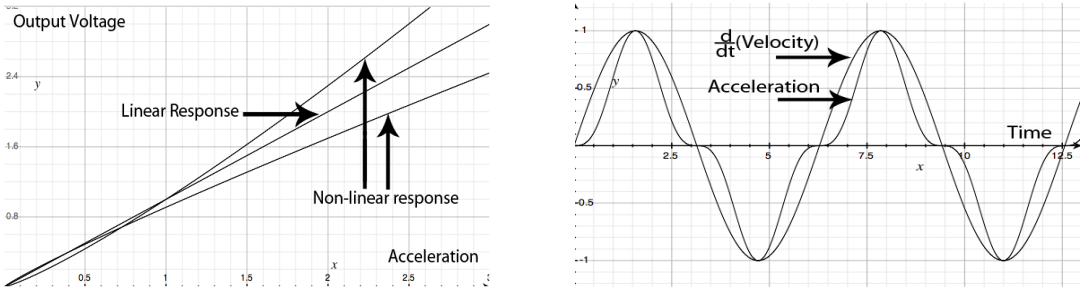

Figure 52 – Possible examples of non-linearity using the testing methods above

In the event that the accelerometer is only sensitive to very high accelerations, two options are available to increase sensitivity. First is to increase the amplification factor. The main issue with this solution is that the signal to noise ratio may drop significantly. Another alternative is to glue lead balls to the proof mass in the accelerometer. This not only increases the overall mass, but also moves the center of gravity, additionally benefiting X and Y acceleration detection. Potential drawbacks include imperfect mass alignment, which can lead to higher cross-axis detection. Figure 4 shows a mass attached to a previously RIT fabricated one axis accelerometer.

Device reliability is a critical measure of performance. The device needs to be both insensitive to shock and extended use. Subjecting the device to short impulses of

high accelerations up to 1000 g will simulate a sudden shock event. Previous devices have incorporated over-range protection to prevent the device from physically breaking [5], showing reliability up to 70,000 g [28]. Long-term reliability can be predicted by accelerated testing under high stress conditions. Devices must be run at excessive supply voltages while being exposed to high levels of acceleration on a PM-Shaker for an extended period of time.

The resonant frequency of the accelerometer is also an important specification, as the device will only operate correctly below this frequency. By applying a square wave acceleration source, the device will naturally oscillate at its resonant frequency.

6.3 Amplification

With sensitivities measured in μV per g of acceleration, high quality amplification it is needed. Figure 53 shows a custom three-channel instrumentation amplifier along with one of several chip carrier boards with an accelerometer attached. Each channel has variable gain and contains the INA101 high precision instrumentation amplifier chip [38]. Gain (G) is given by Equation15, where R_g is the reference variable resistor.

$$G = 1 + \frac{40k\Omega}{R_G} \qquad 15$$

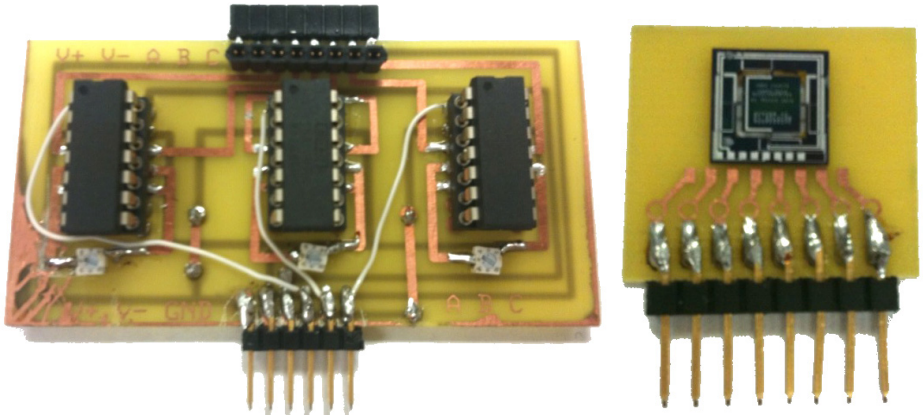

Figure 53 – Custom built three-channel instrumentation amplifier PCB (left) along with one of several carrier boards (right). Each channel has variable gain and contains the INA101 high precision instrumentation amplifier chip [38].

Prior to device testing, each channel of the amplifier has been tested to characterize both gain and linearity. Figure 54 shows the actual gain for each channel based on the value of R_G. All three channels exhibit behavior consistent to Equation 15. Figure 55 shows the frequency response of the amplifier while operating with a gain of 1000 V/V, ensuring that the amplifier works at that gain up to 2 kHz.

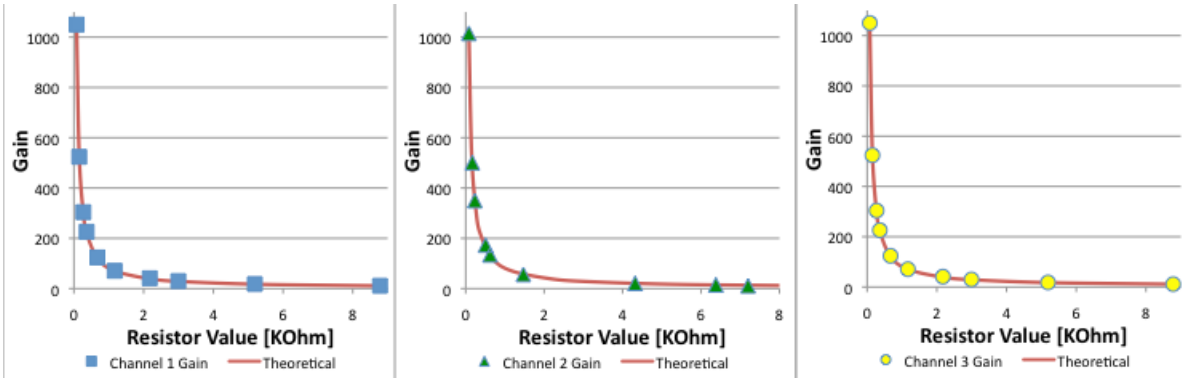

Figure 54 – Gain as a function of reference resistor value for each channel. Follows Equation 15

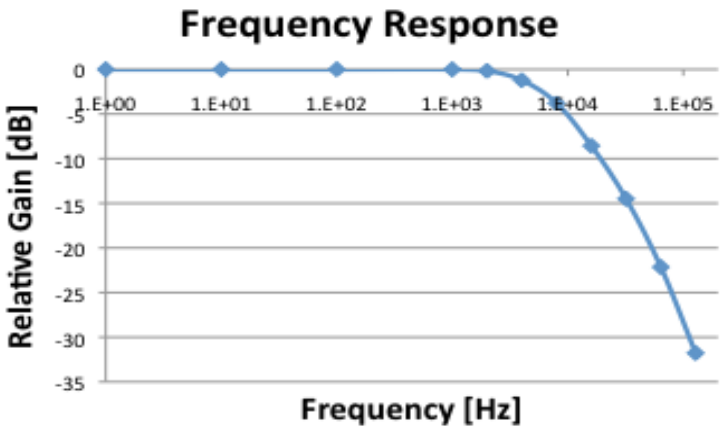

Figure 55 – Frequency response of the amplifier set to 1000X gain. 20dB/decade roll off starts at 2 kHz

6.4 Sensitivity

To test the Wiimote accelerometer for sensitivity, both the Wiimote and iPhone were attached to the speaker setup. Care was taken to align both devices to the speaker face, and then to align the speaker face to earth's gravitational field. The iPhone was arbitrarily chosen as the reference acceleration, and the peak-to-peak accelerations were simultaneously measured at various speaker powers levels with an 8 Hz sinusoidal input signal. Figure 56 shows that the Wiimote has a sensitivity of 2.16 g/g. This is not expected, if both devices are fully calibrated the resulting sensitivity should be 1.00 g/g. Since third party software was used to measure the acceleration levels in each device, the most likely explanation is that one of the software packages incorrectly converts the digital signal to the representative acceleration level.

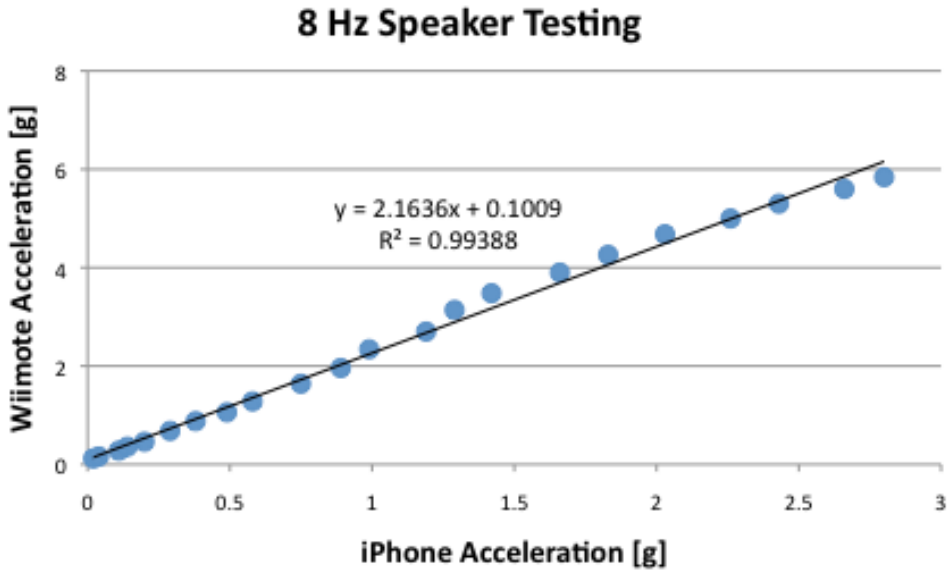

Figure 56 – Wiimote accelerometer measured with reference to the iPhone accelerometer. Measured at 8 Hz on the speaker setup

In addition to sinusoidal input signals, both square wave and half sine impulse trains were recorded at various amplitudes. Figure 57 shows low amplitude 1-millisecond half sine inputs on both accelerometers. This is a representative example of all of the half sine and square wave tests of varying amplitude and frequency. Two things are of interest in these figures. First, even when driving the speaker with low amounts of power, both devices clip at their upper acceleration limits. The iPhone clips at ±2 g of acceleration, while the Wiimote clips at ±3 g. Second, even at the highest data-sampling rate, the event occurs to quickly to accurately plot the response. The iPhone records 100 data points per second, while the Wiimote records 50 points per second. The Analog Devices and ST Microelectronics chips inside are capable of much higher sampling rates, but because Apple and Nintendo have no need for such high sampling rates, they end up limiting to 100 and 50 Hz.

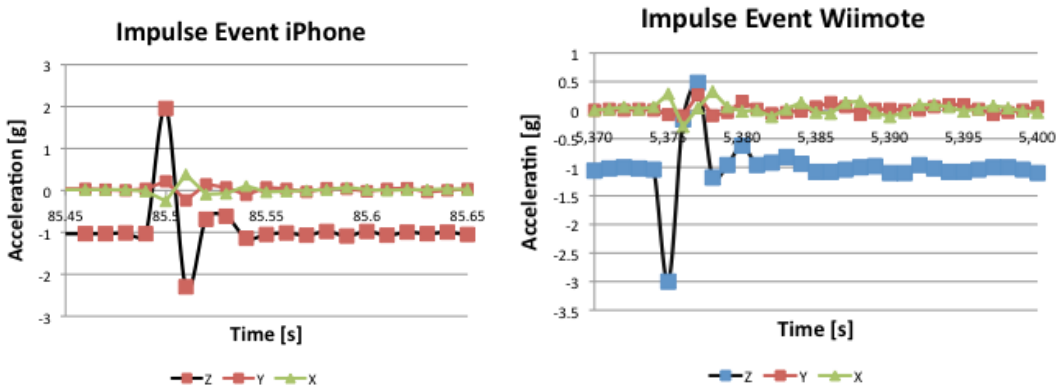

Figure 57 – Impulse event of a half sine wave at 1000 Hz on the iPhone (left) and Wiimote (right).

To get around these issues, the Minisense 100 has been tested against the ADXL278, both having analog voltage outputs. A new issue regarding AC power supply noise was encountered, as shown by the steady state response of the Minisense in Figure 58. Even while stationary, the Minisense shows almost a 700 mV peak-to-peak voltage swing at 60 Hz. This was a result of an AC power cord interfering with the unshielded signal wires. Removing the power cord and adding a 10 MΩ resistor in parallel with the oscilloscope probe reduced the noise to a reasonable level.

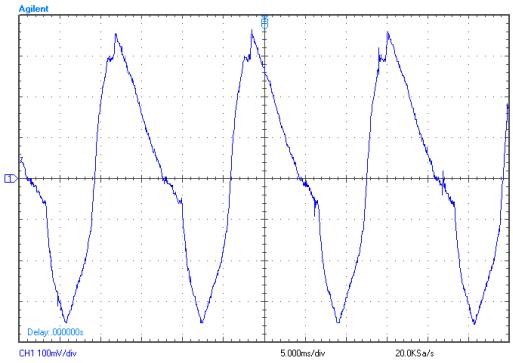

Figure 58 – AC Power noise while measuring the idle Minisense 100.

Both the Minisense and ADXL278 were measured simultaneously on the speaker setup with a constant 40 Hz sinusoidal signal. Figure 59 shows both accelerometer

outputs as a function of speaker signal voltage. After around 20 g of acceleration the ADXL278 still maintains consistent results, but the Minisense starts to exhibit slight signal spiking on the oscilloscope, making accurate peak-to-peak measurements difficult to read.

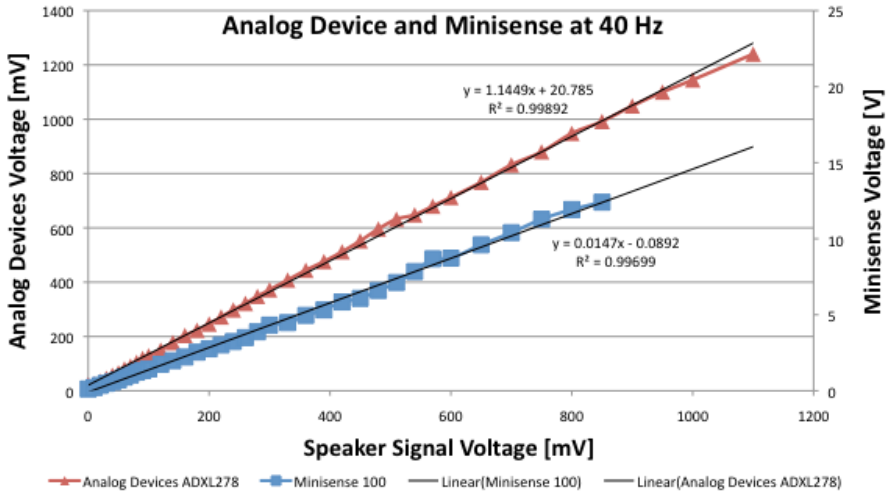

Figure 59 – Output voltages of the Analog Devices ADXL278 and Minisense 100 accelerometers while driven at 40 Hz.

By taking the acceleration of the ADXL278 as a reference, Figure 60 shows the sensitivity of the Minisense to be 0.69 V/g. This is close to the datasheet's expected sensitivity of 1.1 V/g [39], but differs for two main reasons. First, is because of the 10 MΩ resistor placed in parallel with the oscilloscope probe and Minisense. This resistor lowers the overall impedance between the two terminals of the Minisense, allowing for the charge generated by the piezoelectric film to disperse more quickly. Second, is that the datasheet gives an expected sensitivity for low frequency measurements. At 40 Hz, the device is approaching the measured resonant frequency of 63 Hz, discussed later in Chapter 6.7.

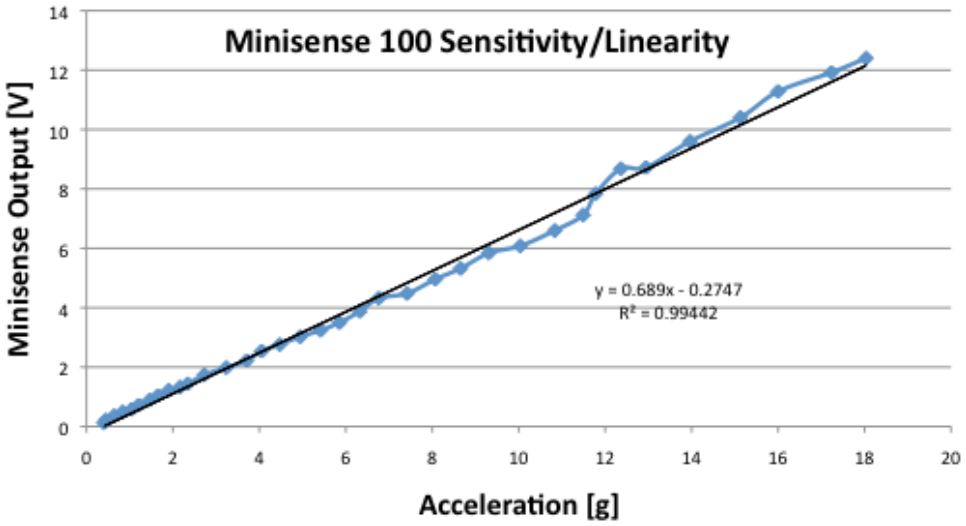

Figure 60 – Minisense 100 sensitivity at 40 Hz

In addition to the speaker test setup, the cantilever test setup can be used for these measurements. Figure 61 shows the iPhone attached to the cantilever, and accelerated to ±2 g peak-to-peak. This cantilever test structure is usually capable of testing ±10g, but the additional weight of the iPhone has slowed down the cantilever beam to a much lower frequency, resulting in lower levels of acceleration.

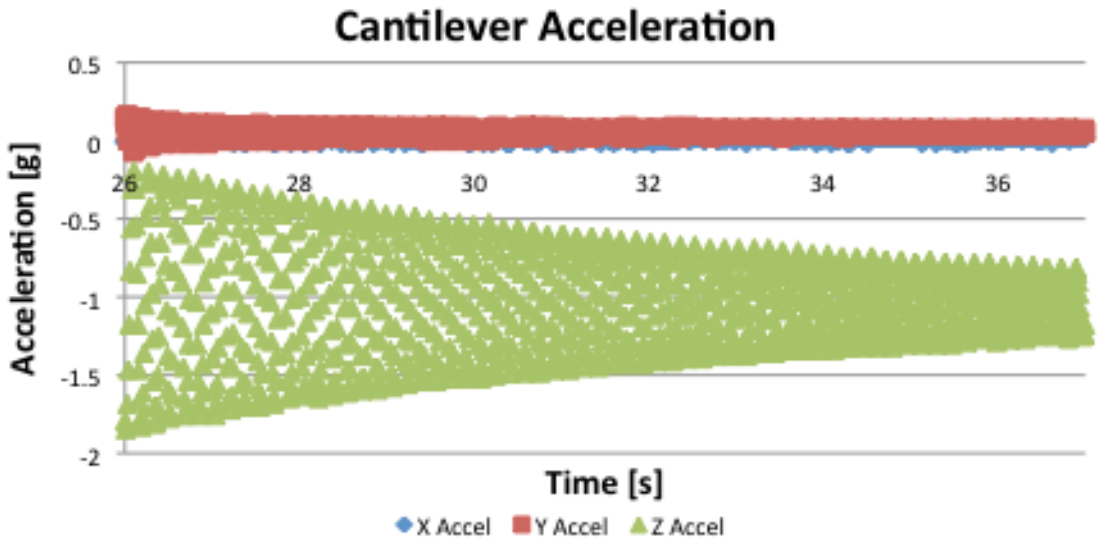

Figure 61 – iPhone under acceleration from the cantilever setup. A truly sinusoidal response is measured. Shown again with a closer view in Figure 62

6.5 Linearity

The Minisense 100 data sheet suggests a linearity of ±1 %. From the data in Figure 60, each data point is an average of 1.02% off of the line of best. When looking at the digital accelerometer data from Figure 56, the average nonlinearity of the Wiimote is 3.61%, much higher than the datasheets predicted value of < 0.2% [40]. This is due to measurement variation, which is especially high around the low g readings where eight bit quantization errors play a large role in measurement error.

One of the proposed methods for measuring linearity involves comparing acceleration to the derivative of velocity. This method assumes a perfectly linear velocity sensor, which is not present in Figure 62. The velocity portion of the graph looks similar to a ramp function, while the measured acceleration looks similar to the expected sine wave.

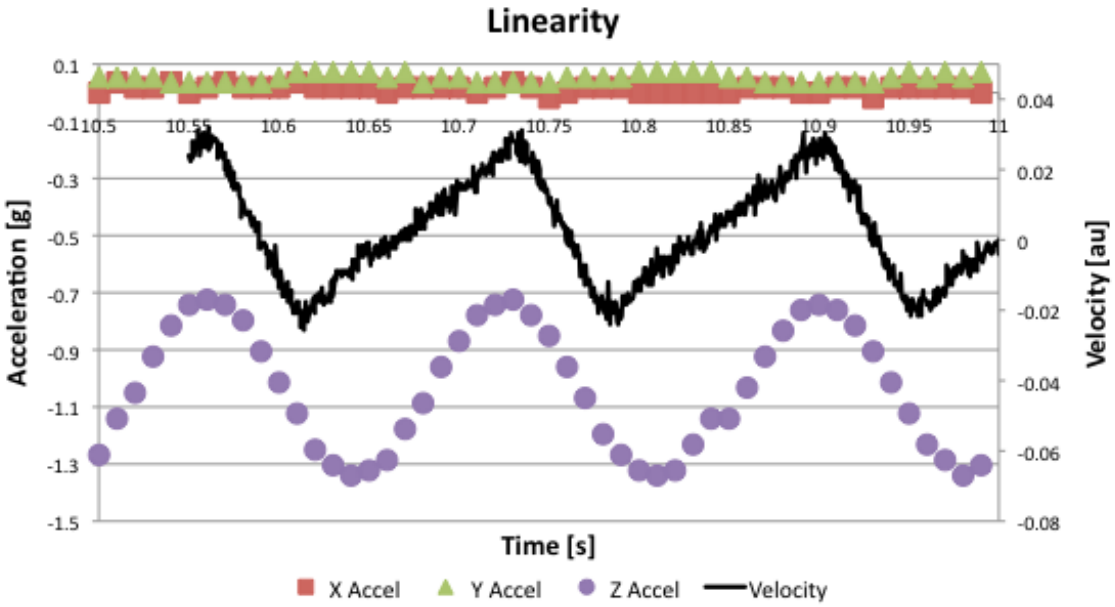

Figure 62 – Acceleration and vertical velocity of the iPhone when tested on the cantilever. Entire plot shown in Figure 61

6.6 Cross-Axis Sensitivity

Independent of any stationary accelerometers orientation, the combined magnitude of the XYZ accelerations should always be 1 g. For the iPhone sitting on a flat table, the average XYZ acceleration values from Figure 63 of 0.032, 0.009, and -1.033 g give a combined magnitude of 1.034 g, 3.4% larger than expected. This could be caused by axis cross talk, where acceleration in one direction is also measured in the other two directions. This could also be caused by poor software data conditioning, as the LIS331DL sensor predicts < 1.0% axis cross talk [41].

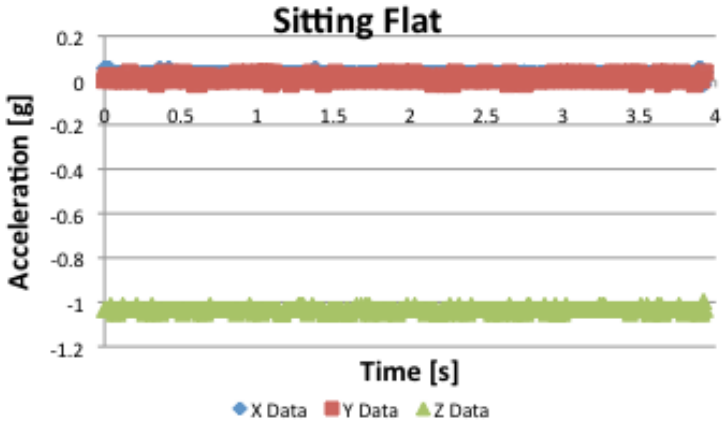

Figure 63 – Acceleration measurements of the iPhone sitting flat on a level table

Figure 64 shows measurements taken to calculate the axis cross talk while rotating the device over the Y-axis (top) and X-axis (bottom). On the left side acceleration is plotted over a two second rotation period. On the right the overall magnitude minus 1 g of acceleration is plotted over the same time frame. Theoretically this should yield 0 g, independent of time. The graphs, however, show that this is not the case. Rotating around the Y-axis yields an average cross-talk level of 3.18%, while rotating around the X-axis yields an average of 0.67%. This may be partially due to the acceleration caused by physically rotating the device. Care was given to rotate slowly and

around the center of the accelerometer, but even small amounts of rotational acceleration can be picked up during the measurement.

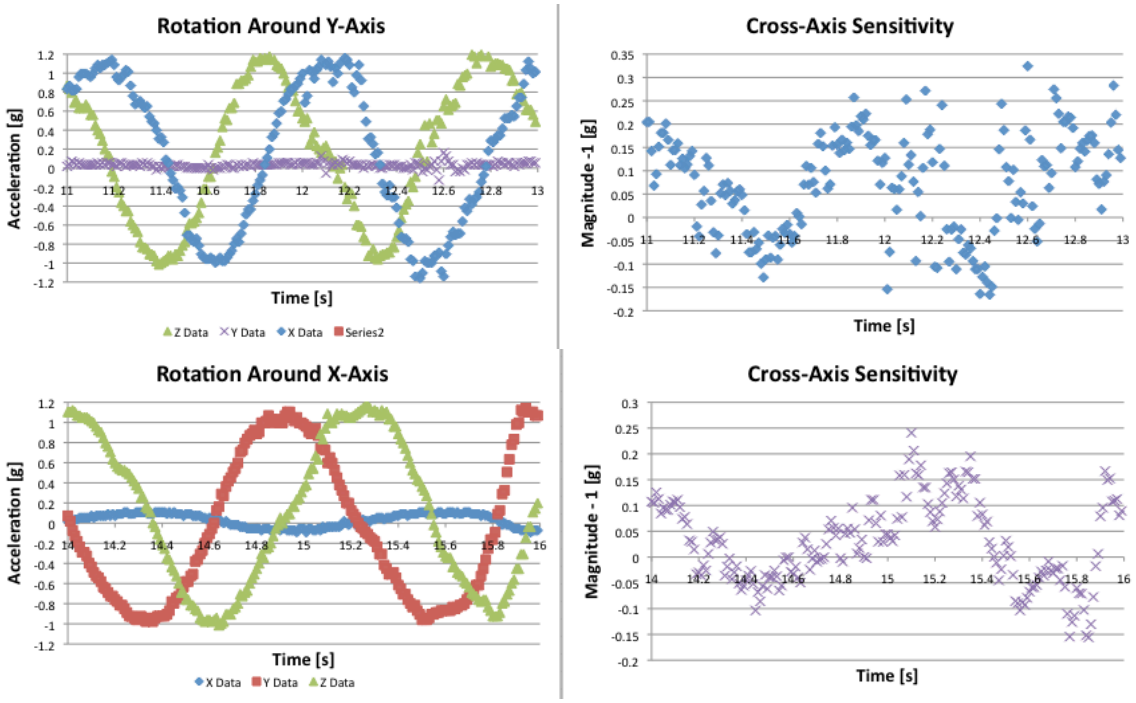

Figure 64 – Acceleration measurements (left) and cross-axis sensitivity levels (right) of the iPhone being rotated around the y-axis (top) and x-axis (bottom)

In addition to axis cross talk associated with the sensor itself, the testing setup can actually introduce additional cross talk. Improper alignment of the accelerometer to the speaker or cantilever structure will result in all three of the axes showing acceleration when the test structure is actuated. The amount of acceleration is proportional to the sine of the misalignment error, so even small amounts of misalignment are measurable. If the accelerometer is not properly fastened down, stray resonant vibrations can cause the accelerometer to read acceleration in unintended axes.

After attaching the Wiimote and iPhone accelerometers to the speaker in Figure 65, steady state values show misalignment to earth's gravitational field. Calculations

show a gravitational alignment error of 0.85° around the Y-axis and 1.23° around the X-axis. This can be corrected for by adjusting the accelerometers and speaker until the X and Y axes show no acceleration and the Z axis shows the full 1 g of acceleration.

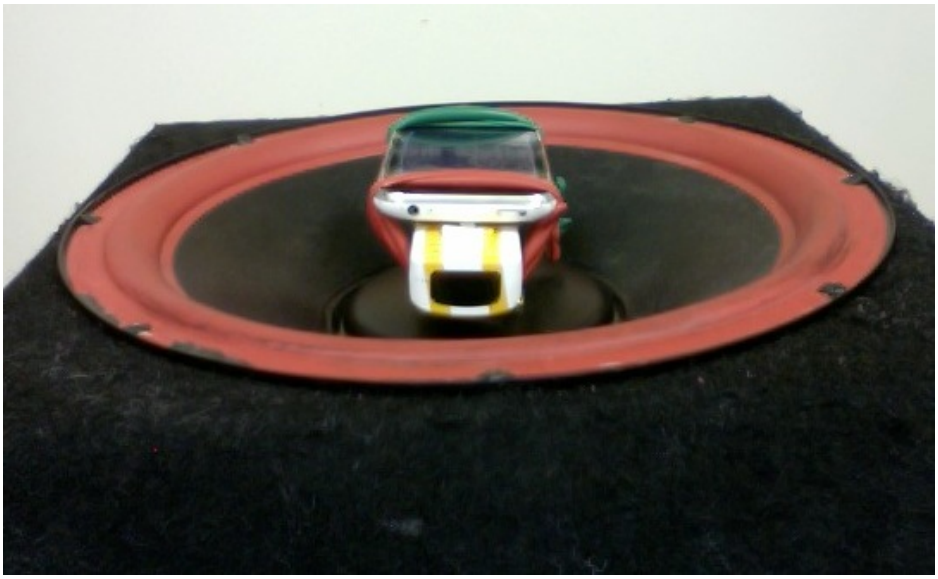

Figure 65 – Speaker with attached Nintendo Wiimote and Apple iPhone

Even with all precautions taken, the cantilever test structure can naturally introduce axis cross talk at high amplitudes due to it's movement nature. This is shown in Figure 66, where the initial XY coordinate systems shifts to an X'Y' system once the beam starts to move. With dimensions of L = 45 cm and H = 1 cm, the resulting angle Θ is equal to 1.27°. At the peak amplitude, where acceleration is at a maximum, this should result in the accelerometer reading an X value 2.2 % of the total acceleration. Experimental data shows the maximum X acceleration to be 6.6% of the total acceleration, indicating that the accelerometer was misaligned around the Z-axis by around 4.4°. Maximum acceleration in the Z direction was 2.0% of the total acceleration, indicating a misalignment around the X-axis of 1.1°.

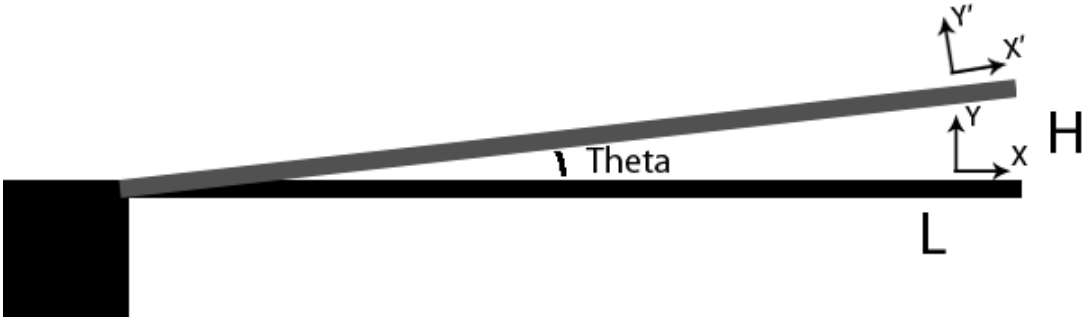

Figure 66 – Cantilever introducing axis cross talk at high amplitudes

6.7 Frequency Response

All of the commercial accelerometers except the Minisense have built in filters to prevent outputs at or past their resonant frequency, typically in the 500-5000 Hz range. The Minisense, however, can be tested against frequency because it has no built in filters. Figure 67 shows the expected frequency response from the manufacturer's datasheet, which predicts a resonant frequency around 75 Hz [39].

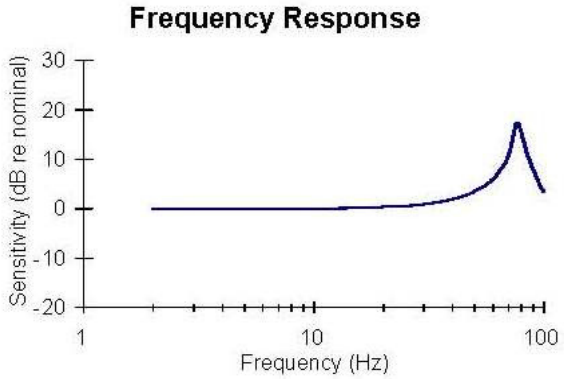

Figure 67 – Frequency response of the Minisense accelerometer as shown by the manufacturer [39]

Figure 68 shows the measured frequency response while using a low amplitude sinusoidal signal on the speaker setup. The actual resonant frequency is measured to be 61 Hz, lower than the data sheet predicts. One reason this is off is that the test actually confounds the frequency response of the speaker into the measured frequency response of

the Minisense. The speaker used is a car sub-woofer, which has its own resonant frequency somewhere in the bass range, below 100 Hz.

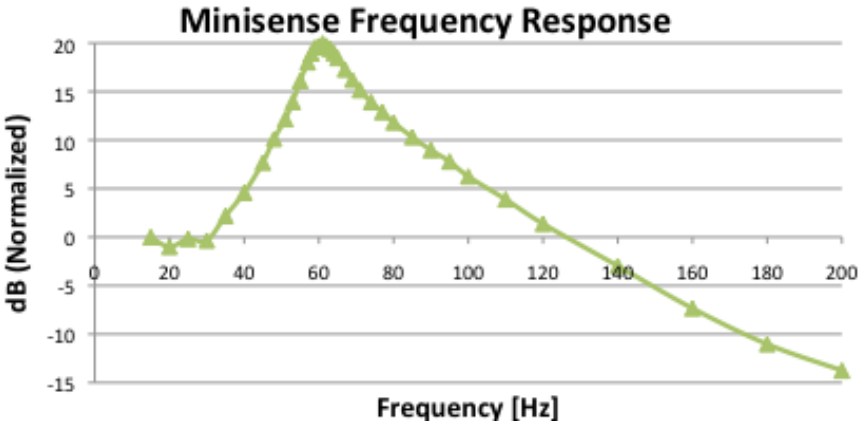

Figure 68 – Measured frequency response of the Minisense accelerometer. Resonance occurs at 61 Hz. Tested on the speaker setup with 100 mV of sinusoidal input

When stimulating an accelerometer with a square wave, it will naturally vibrate at its resonant frequency. Figure 69 shows the Minisense excited with a high amplitude square wave. Measuring the time between several cycles reveals a more accurate resonant frequency of 63 Hz.

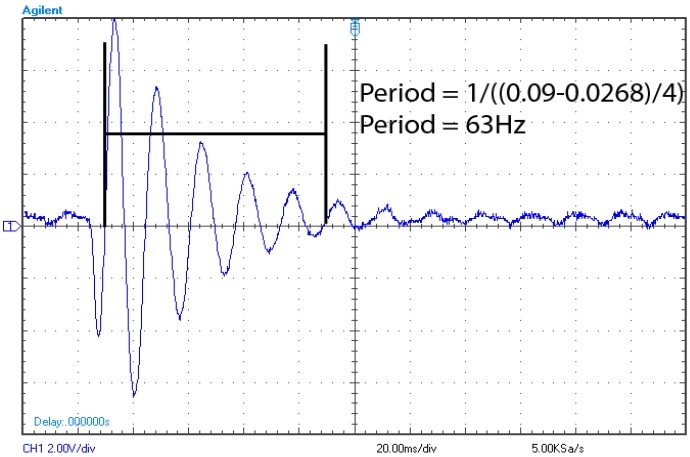

Figure 69 – Impulse on the Minisense reveals a resonant frequency of 63 Hz

The frequency response of the speaker setup with the attached iPhone and Wiimote is shown in Figure 70. A constant low power sinusoidal input was used, with frequencies varying from 1 to 120 Hz. As shown before, the iPhone outputs around twice the acceleration of the Wiimote.

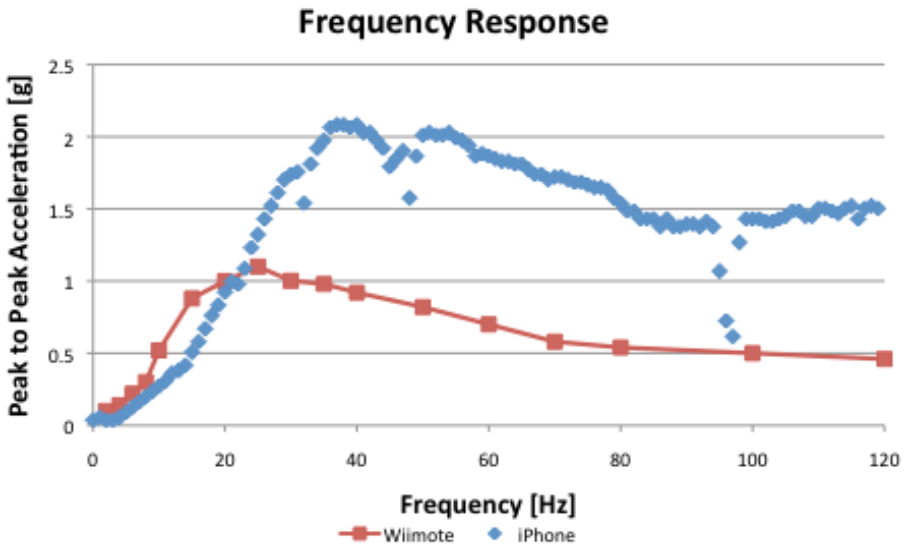

Figure 70 – Frequency response of the speaker-accelerometer system. iPhone shows distinct beats near the half and full sampling frequency, as shown in Figure 71.

Two interesting result from the iPhone frequency response are the dips, one near 49 Hz and another near 96 Hz. This is due to the low sampling rate of 100 Hz. Figure 71 shows the acceleration as the frequency was scanned from 1 to 120 Hz over a 120 seconds interval. Around the sampling frequency of 100 Hz and the half frequency of 50 Hz, the same part of the sin wave was sampled at every point. This gives the false impression of low peak-to-peak voltages, the Wiimote graph in Figure 70 gives a better picture of the frequency response. This issue can be solved with higher sampling rates.

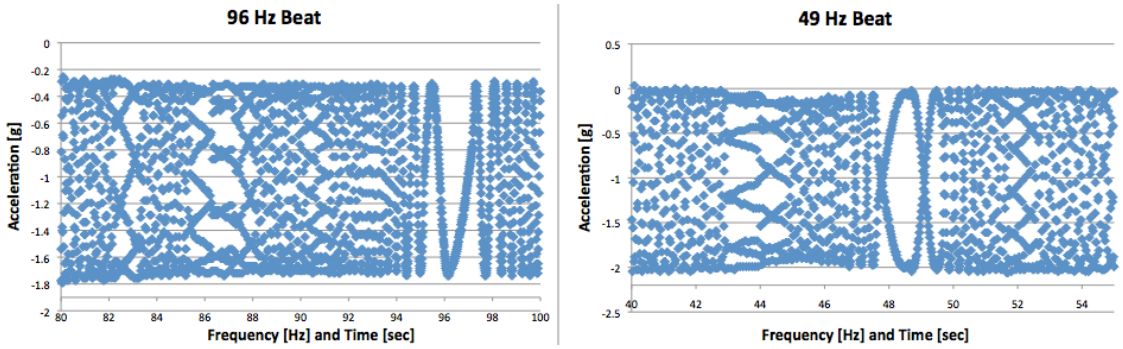

Figure 71 – Beats near the sampling frequency (100 Hz), distorting the frequency response results.

6.8 Mechanical Stability

To test mechanical stability, the Minisense 100 was placed on the speaker setup and continually run for twenty-four hours. A large sinusoidal signal was fed to the speaker at the resonant frequency of 63 Hz, resulting in initial peak-to-peak accelerations of 51.6 ± 0.8 g. After twenty-four hours the accelerometer showed 52.4 ± 0.8 g of acceleration. Both responses are shown in Figure 72, and both responses are consistent within the margin of error. These results are expected as there are no known degradation mechanisms at work, such as hot carrier effects in MOSFETs [42]. This is true only if the accelerometer is working in the elastic deformation range.

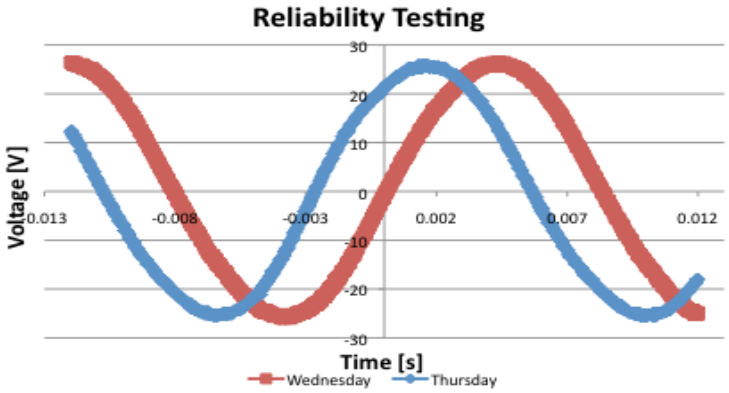

Figure 72 – Output voltage of the Minisense accelerometer while excited at ±23.6 g for 24 hours. No difference measured

Chapter 7

Conclusion

7.1 Introduction

Several accelerometers were designed, simulated, and fabricated from the fall of 2009 through the summer of 2010. While no fully working devices were demonstrated, commercial accelerometers were tested so that the procedures could be reproduced with devices fabricated in the future. The processing knowledge gained will be invaluable for future projects using the RIT bulk MEMS process, and is not just limited to benefiting accelerometers. Even though processing issues prevented the chips from working, the accelerometer designs are still believed to be solid.

7.2 Future Work

After correctly fabricating working devices, future work could include scaling the die size down from 10 mm square to 2-4 mm square. Scaling the critical dimension down from 10 μm would require processing improvements at every step, but a small die size is still possible with a critical dimension of 10 μm if the proof mass size is reduced. Several processing steps still need improvement, mostly relating to the aluminum interconnects and diaphragm etch. Additionally, integrating a CMOS amplifier onto the chip would eliminate the need for a custom instrumentation amplifier board, reducing integration cost and complexity. The testing techniques used on the four tested accelerometers could also be used to characterize the backup ADXL330 and BMA140 chips. A printed circuit board has already been designed, shown in Figure 73.

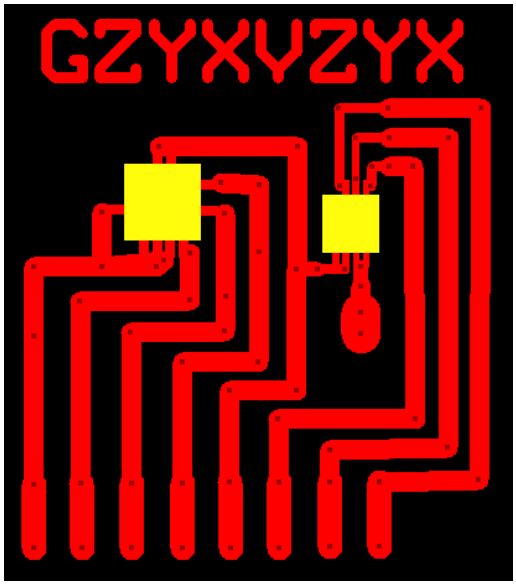

Figure 73 – PCB Schematic to test the Analog Devices ADXL330 and Bosch BMA140 accelerometers

Jake Leveto received his Bachelor's degree in Microelectronic Engineering from the Rochester Institute of Technology in May 2010 and his Masters in microelectronic engineering with Dr. Lynn Fuller in June 2010. Jake has cooped for Eastman Kodak working on organic LED displays, and for his own business that produces 3D games for the Macintosh and iPhone. Jake plans on moving back to Meadville Pennsylvania to work full-time on his own business and travel before searching for employment in the microelectronics field.

Chapter 8

Appendices

Appendix 1 - RIT Bulk MEMS Process Flow

Process Step	Time	Rate	Total	Process Step	Time	Rate	Total
1 Obtain qty 10, 4" n-type wafers	10	$15	$150	31 PlasmaEtchNitrideonbackofwaf	1.5	$75	$113
2 Wafer grind to 300um	4	$75	$300	32 1.5min 10:1 HF to remove Pac	0.25	$50	$13
3 Polish back side	3	$75	$225	33 Remove resist - solvent strip 5	0.5	$0	$0
4 CMP Clean	0.5	$50	$25	34 RCA Clean	1	$50	$50
5 RCA Clean	1	$50	$50	35 Deposit 6000Å Poly LPCVD	3	$70	$210
6 Grow masking oxide 5000 Å, Recip	4	$32	$129	36 Spin on Glass, N-250	1	$16	$16
7 Photo 1: P+ diffusion	4	$33	$133	37 Poly Diffusion, Recipe 120	3	$32	$97
8 Etch Oxide, 12 min, Rinse, SRD	0.5	$50	$25	38 Etch SOG	0.5	$50	$25
9 Strip Resist	0.5	$0	$0	39 4 pt Probe	0.25	$0	$0
10 Spin-on Glass, Borofilm 100, incl	1	$16	$16	40 Photo 3, Poly	4	$33	$133
11 Dopant Diffusion Recipe 110	4	$32	$129	41 Etch poly, LAM490	1.5	$75	$113
12 Etch SOG and Masking Oxide, 20	0.5	$50	$25	42 Strip resist	0.5	$0	$0
13 Four Point Probe Dummy Wafer	0.5	$0	$0	43 RCA Clean	1	$50	$50
14 RCA Clean	1	$50	$50	44 Oxidize Poly Recipe 250	3	$33	$98
15 500Å Pad Ox - recipe 250	4	$32	$129	45 Deposit 8,000Å TEOS or LTO C	3	$70	$210
16 Deposit 1500Å Nitride	2	$70	$140	46 Photo 4, Contact Cut	4	$33	$133
17 Coat back of wafer and protect e	1	$55	$55	47 Etch Oxide in BOE, Rinse, SRD	0.5	$50	$25
18 PlasmaEtchNitrideonfrontofwafer	1.5	$75	$113	48 Strip Resist	0.5	$0	$0
19 Strip backside resist	0.5	$0	$0	49 RCA Clean, include extra HF st	1	$50	$50
20 Remove pad oxide - 1min BOE	0.25	$50	$13	50 Deposit Aluminum, 10,000Å	1.5	$34	$51
21 RCA Clean	1	$50	$50	51 Photo 5, Metal	4	$33	$133
22 Grow 5,000Å of oxide - recipe 35	4	$32	$129	52 Etch Aluminum, Wet Etch	0.5	$50	$25
23 Photo 6: N+ diffusion	4	$33	$133	53 Strip Resist	0.5	$0	$0
24 Etch oxide	0.5	$50	$25	54 Deposit 10,000Å LTO Oxide Pa	3	$70	$210
25 N+ SOG	1	$16	$16	55 Photo 6, Via	4	$33	$133
26 Strip resist, RCA clean	1	$50	$50	56 Via etch - pad etch 8 min	0.25	$50	$13
27 N+ drive -in	4	$32	$129	57 Ash resist	1	$39	$39
28 Photo 2: Backside Diaphragm	4	$33	$133	58 Spin coat PROTEK on front of	1	$55	$55
29 Coat front of wafer and protect e	1	$55	$55	59 Etch Diaphragm in KOH, ~4 h	4	$50	$200
30 Etchoxynitride,1min10:1HF	0.25	$50	$13	60 Strip PROTEK	1	$39	$39
				61 Test	0	$0	$0

Materials	#	Rate	Total
Masks	7	$440	$3,080

Processing	$4,670.70
Materials	$3,080.00
Grand Total	$7,750.70

Appendix 2 – Full bridge behavior under all acceleration conditions

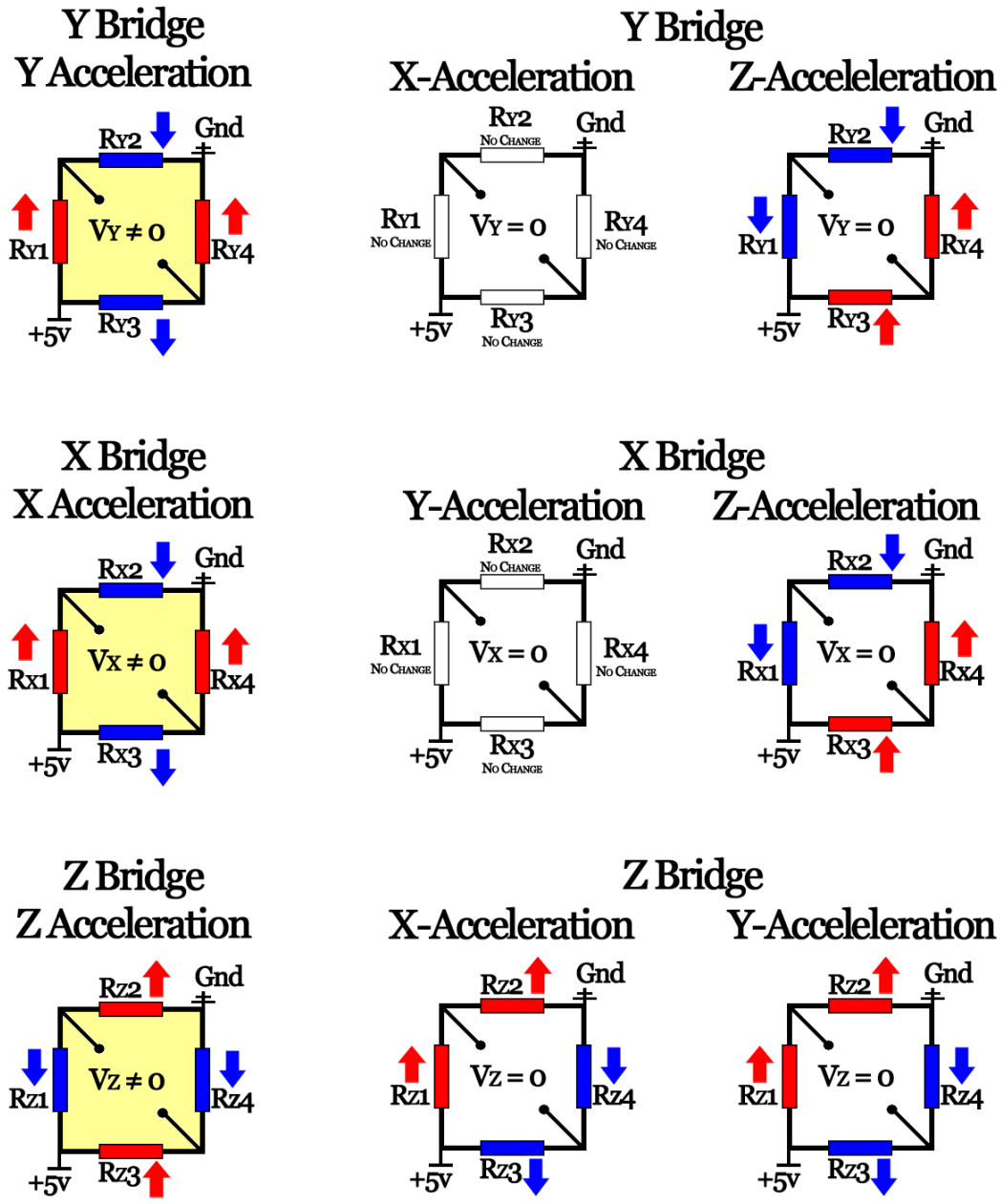

Appendix 3 – Silvaco Athena Simulations

```
#Initialize
line x loc=0.00 spac=0.3
line x loc=20 spac=0.3
line y loc=0.00 spac=0.015
line y loc=2.00 spac=0.15
init silicon c.phosphor=2.0e15 orientation=100

#Mask oxide 5000a
diffus time=100 temp=1000 weto2
etch oxide start x=5.0 y= -2.0
etch cont x=5.0 y= 2.0
etch cont x=15.0 y= 2.0
etch done x=15.0 y= -2.0

#Implant/Grow Alignment Mark
implant boron dose=3.0e14 energy=90 tilt=7 rotation=45 crystal
diffus time=54 temp=1000 dryo2
etch oxide all
extract name="Rs" p.sheet.res material="Silicon" mat.occno=1 x.val=10 region.occno=1

#Nitride Pad oxide
diffus time=54 temp=1000 dryo2
etch oxide all

#5000A oxide recipe 353 (350 added here)
diffus time=100 temp=1000 weto2

#Poly doping
diffus time=15 temp=1000 nitro

#Poly oxidation
diffus time=54 temp=1000 dryo2

#Extraction
extract name="Oxide" thickness material="Oxide" mat.occno=1 x.val=10
extract name="Resistance" p.sheet.res material="Silicon" mat.occno=1 x.val=10
region.occno=1

etch oxide start x=5.0 y= -2.0
etch cont x=5.0 y= 2.0
etch cont x=15.0 y= 2.0
etch done x=15.0 y= -2.0

tonyplot
```

Appendix 4 – Micrograph of the three-axis accelerometer

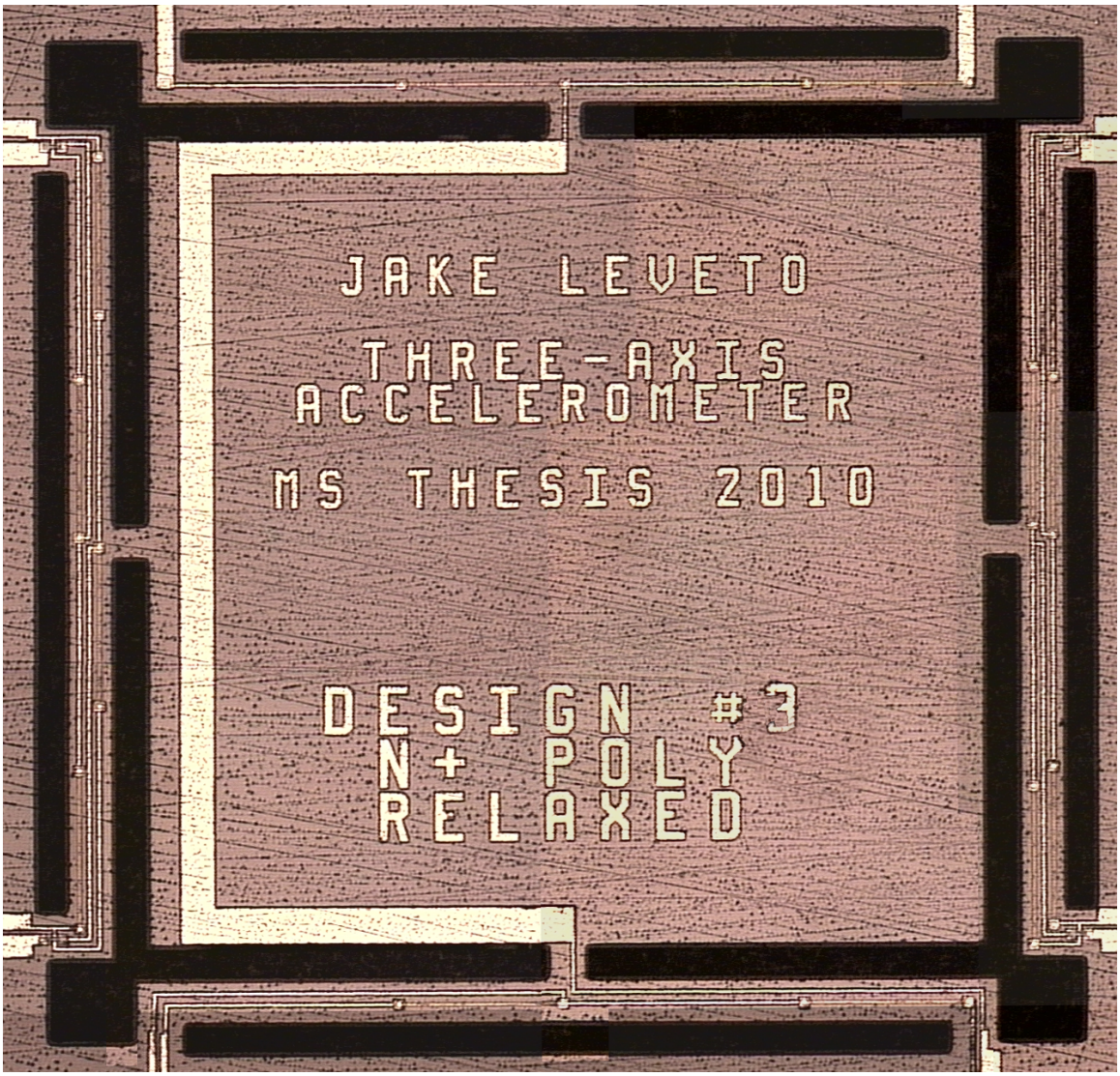

REFERENCES

[1] N. Yazdi, F. Ayazi, and K. Najafi, "Micromachined inertial sensors," *Proceedings of the IEEE,* vol. 86, no. 8, pp. 1640-1659, 1998.

[2] L. Fuller, and I. Puchades. "Bulk Micromachined Laboratory Project," http://people.rit.edu/lffeee/MEM_BULK_2007-Spring_Process.pdf.

[3] J. McGovernm, and N. NAVAIR, "Analysis of Prognostic Sensor Technologies for MEMS Applications in Military Systems," 5/18/2009, 2009.

[4] R. Stewart, R. Thede, P. Couch *et al.*, "High G MEMS accelerometer for Compact Kinetic Energy Missile (CKEM)." pp. 20-25.

[5] H. Xie, G. K. Fedder, and R. E. Sulouff, "Accelerometers," *Comprehensive Microsystems*, G. Yogesh, T. Osamu and Z. Hans, eds., pp. 135-180, Oxford: Elsevier, 2008.

[6] B. Baylav, I. Puchades, S. Lyshesvski *et al.*, "MEMS Accelerometer Laboratory," 2008.

[7] H. Takao, H. Fukumoto, and M. Ishida, "A CMOS integrated three-axis accelerometer fabricated with commercial submicrometer CMOS technology and bulk-micromachining," *Electron Devices, IEEE Transactions on,* vol. 48, no. 9, pp. 1961-1968, 2001.

[8] E. J. S. Eklund, Andrei M., "Single-mask fabrication of high-G piezoresistive accelerometers with extended temperature range," *Multi-Campus*, 4/1/2007.

[9] L. M. Roylance, and J. B. Angell, "A batch-fabricated silicon accelerometer," *Electron Devices, IEEE Transactions on,* vol. 26, no. 12, pp. 1911-1917, 1979.

[10] K. Kwon, and S. Park, "A bulk-micromachined three-axis accelerometer using silicon direct bonding technology and polysilicon layer," *Sensors and Actuators A: Physical,* vol. 66, no. 1-3, pp. 250-255, 1998.

[11] S. Kal, S. Das, D. K. Maurya *et al.*, "CMOS compatible bulk micromachined silicon piezoresistive accelerometer with low off-axis sensitivity," *Microelectronics Journal,* vol. 37, no. 1, pp. 22-30, 2006.

[12] D. V. Dao, S. Okada, V. T. Dau *et al.*, "Development of a 3-DOF silicon piezoresistive micro accelerometer." pp. 271-276.

[13] R. Amarasinghe, D. V. Dao, T. Toriyama *et al.*, "Development of miniaturized 6-axis accelerometer utilizing piezoresistive sensing elements," *Sensors and Actuators A: Physical,* vol. 134, no. 2, pp. 310-320, 2007.

[14] J. A. Plaza, H. Chen, J. Esteve *et al.*, "New bulk accelerometer for triaxial detection," *Sensors and Actuators A: Physical,* vol. 66, no. 1-3, pp. 105-108, 1998.

[15] H. Chen, M. Bao, H. Zhu *et al.*, "A piezoresistive accelerometer with a novel vertical beam structure," *Sensors and Actuators A: Physical,* vol. 63, no. 1, pp. 19-25, 1997.

[16] L. Fuller, B. Baylav, and I. Puchades, "Various MEMs Accelerometer Designs Using a Bulk Silicon Process ", April 2007.

[17] S. E. Thompson, M. Armstrong, C. Auth *et al.*, "A 90-nm logic technology featuring strained-silicon," *Electron Devices, IEEE Transactions on,* vol. 51, no. 11, pp. 1790-1797, 2004.

[18] C. S. Smith, “Piezoresistance Effect in Germanium and Silicon,” *Physical Review,* vol. 94, no. Copyright (C) 2010 The American Physical Society, pp. 42, 1954.
[19] Y. Kanda, “A graphical representation of the piezoresistance coefficients in silicon,” *Electron Devices, IEEE Transactions on,* vol. 29, no. 1, pp. 64-70, 1982.
[20] C. Mazure, and I. Cayrefourcq, "Status of device mobility enhancement through strained silicon engineering." pp. 1-6.
[21] A. A. Barlian, W. T. Park, J. R. Mallon *et al.*, “Review: Semiconductor Piezoresistance for Microsystems,” *Proceedings of the IEEE,* vol. 97, no. 3, pp. 513-552, 2009.
[22] S. Changzhi, L. Xiaowei, and C. Rongyan, "Piezoresistive linearity analysis of polysilicon nanofilms deposited at different temperatures based on interstitial-vacancy model." pp. 799-802.
[23] Q. Hongwei, F. Deyou, and X. Huikai, “A Monolithic CMOS-MEMS 3-Axis Accelerometer With a Low-Noise, Low-Power Dual-Chopper Amplifier,” *Sensors Journal, IEEE,* vol. 8, no. 9, pp. 1511-1518, 2008.
[24] J. M. Bustillo, R. T. Howe, and R. S. Muller, “Surface micromachining for microelectromechanical systems,” *Proceedings of the IEEE,* vol. 86, no. 8, pp. 1552-1574, 1998.
[25] K. C. S. Adel S. Sedra, *Microelectronic Circuits*, Revised ed.: Oxford University Press, 2007.
[26] AnalogDevices. "Low g Accelerometers," February 8th, 2010; http://www.analog.com/en/mems/low-g-accelerometers/products/index.html.
[27] AnalogDevices. "High g Accelerometers," February 8th, 2010; http://www.analog.com/en/mems/high-g-accelerometers/products/index.html.
[28] A. Beliveau, G. T. Spencer, K. A. Thomas *et al.*, “Evaluation of MEMS capacitive accelerometers,” *Design & Test of Computers, IEEE,* vol. 16, no. 4, pp. 48-56, 1999.
[29] A. R. Sankar, V. Saini, S. Das *et al.*, "Temperature drift analysis in silicon micromachined piezoresistive accelerometer." pp. 561-563.
[30] I. Puchades, *MEMS Processing Update*, RIT, Rochester, NY, 2010.
[31] R. T. Stanley Wolf, *Silicon Processing For the VLSI Era*, 1 ed., p.^pp. 367-372: Lattice Press, 1986.
[32] BrewerScience. "ProTEK(R) B3 Wet-Etch Protective Coating," 5/24/2010, 2010; http://www.brewerscience.com/products/protek/wet-etch-protective-coating/.
[33] M. D. D. James D. Plummer, Peter B. Griffin, *Silicon VLSI Technology*, 1 ed.: Prentice Hall, 2000.
[34] InnovativeApplications. "AccelPlot and MagPlot," 2010; http://innapps.com/accelAndMagPlot.php.
[35] SourceForge, “Get DarwiinRemote at SourceForge.net,” 2008.
[36] P. P. I. Robert D. Sill, “Accelerometer Transverse Sensitivity Measurement Using Planar Orbital Motion,” 11/3/2006, 2006.
[37] AnalogDevices. "ADXL278: Dual-AXIS, HIGH-G, IMEMS® ACCELEROMETER," http://www.analog.com/en/sensors/inertial-sensors/adxl78/products/product.html.

[38] TexasInstruments, "High Accuracy Instrumentation Amplifier (INA101)," *Texas Instruments*, T. Instruments, ed., 2000.
[39] MeasurementSpecialties, "MiniSense 100 Vibration Sensor," 2008.
[40] AnalogDevices, "Small, Low Power, 3-Axis ±5 g Accelerometer," 2009.
[41] STMicroelectronics, "MEMS motion sensor 3-axis - ±2g/±8g smart digital output “nano” accelerometer," 2008.
[42] Y. Tsividis, *Operation and Modeling of The MOS Transistor*, 2 ed.: Oxford University Press, 2003.